CONTROLLED BLASTING CALCULATIONS WITH THE TENSOR74 CODE

M. Heusinkveld
J. Bryan
D. Burton
C. Snell

Februarv 24, 1975

Prepared for U.S. Energy Research & Development Administration under contract No. W-7405-Eng-48

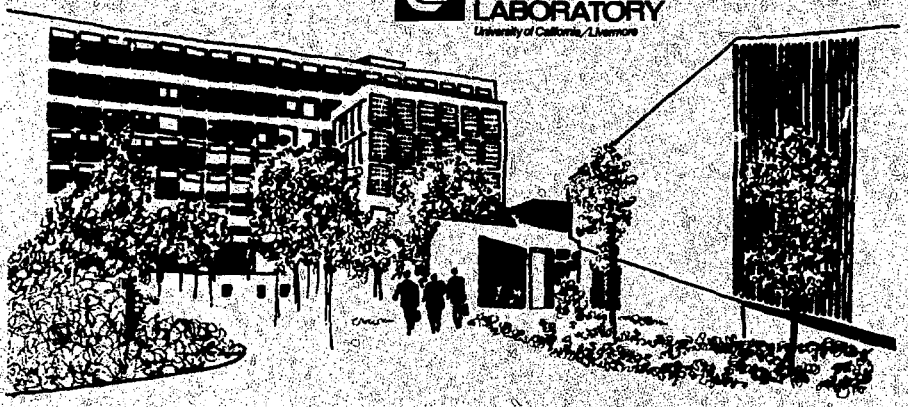

Printed in the United States of America
Available from
National Technical Information Service
U. S. Department of Commerce
5285 Port Royal Road
Springfield, Virginia 22151
Price: Printed Copy $___*; Microfiche $2.25

*Pages	NTIS Selling Price
1-50	$4.00
51-150	$5.45
151-325	$7.60
326-500	$10.60
501-1000	$13.60

TID-4500, UC-35
Peaceful Application
of Explosions

LAWRENCE LIVERMORE LABORATORY
University of California/Livermore, California/94550

UCRL-51740

CONTROLLED BLASTING CALCULATIONS WITH THE TENSOR74 CODE

M. Heusinkveld
J. Bryan
D. Burton
C. Snell

MS. date: February 24, 1975

Contents

CONTROLLED BLASTING CALCULATIONS WITH THE TENSOR74 CODE

Abstract

This report presents the results of numerical finite-difference calculations designed to simulate the effects of blasting explosives emplaced in medium-strength rock. Calculations were implemented using the TENSOR74 two-dimensional rock mechanics code, which models regimes of material response including explosive energy release (detonation), gas expansion, elastic solid material, and brittle or ductile failure of a solid. The standard configuration consisted of a narrow vertical cylinder of explosive within a sandstone medium, beneath a horizontal free surface. The geometry and explosive depth were selected to simulate typical blasting applications. The standard explosive was nitromethane, which was initiated from the lower end.

Variations from this design were made in additional calculations, including top initiation of the explosive, use of ammonium nitrate fuel oil explosive instead of the nitromethane, and reduction of the tensile strength of the sandstone. Frictionless slip surfaces and buffer zones of precrushed sandstone were also added to investigate the influence of presplit fracture planes as used commercially and of buffer zones to control the region-of-rock failure around the explosive.

Propagation of the outgoing dilatational and shear waves was observed with the aid of the TENPLT graphical output program. The extent of the region of failure and the degree of damage in the sandstone medium were examined. A study was made of the states of pressure and deviatoric stress associated with failure at various locations in the rock. It was found that near the explosive the rock failed in shear at high confining pressure, but farther away the rock failed in tension, with long progressive cracks reaching out radially. The extent of these cracks was found to be highly dependent upon the tensile strength assumed for the rock.

Introduction

The efficient use of high explosives as an excavation tool requires the ability to predict and control the location and degree of rock fracturing. In conventional practice, explosive emplacement designs have been established by means of empirical field tests for rock type and explosive.[1,2] Sophisticated controlled blasting techniques, which utilize smaller subsidiary detonations and presplit planes to control overbreak and to precisely fix the cut dimensions, have also been

developed with a largely empirical approach. The few analytic and experimental studies conducted in the past have been somewhat descriptive in nature because of the inability to precisely model or measure the high-pressure inelastic rock behavior and complex stress histories near an explosive detonation.

The application of finite-difference computer programs offers a means to overcome these difficulties and to place blasting design on a more reliable basis. Recognizing the need for improved controlled blasting technology and the potential of these computer programs for simulating high-explosive blasting effects, the U.S. Army Corps of Engineers Explosive Excavation Research Laboratory (EERL) proposed a comprehensive four-phase research program to the National Science Foundation. The first phase involved hydrodynamic code calculations to simulate controlled blasting in a particular geometry. Upon award of a research grant, EERL arranged for calculational support from the Lawrence Livermore Laboratory (LLL), Earth Sciences Division. Additional financial support has been received from the U.S. Energy Research & Development Administration. The program plan for the grant and a description of the computer codes were presented at a conference on excavation technology.[4] This report summarizes the results of these calculations, and analyzes them in terms of the various interacting stress waves.

The computational methods are capable of modeling regimes of material behavior that include explosive energy release, fluid flow, elastic solid, and plastic flow or brittle failure of a solid.[5,6] Available codes include SOC73[7,8] (one-dimensional spherical, planar, or cylindrical symmetry) and TENSOR74[9-12] (two-dimensional spherical, planar, or cylindrical symmetry), which were used to calculate phenomena such as high-explosive and nuclear cratering, and stress-wave propagation and rock fracturing from contained nuclear detonations.[13-17]

The rock mechanics models used in these codes have undergone considerable recent development incorporating improved failure and damping descriptions. These physical models, previously developed for the SOC73 code, have been integrated into the two-dimensional TENSOR code as part of the current research effort. The new two-dimensional code has been used for the calculations described in this report. Along with this modified calculational code, an improved output code (TENPLT) has been used to present the results of the two-dimensional calculations in a graphic format.[18]

The TENSOR74 Code

The TENSOR74 code is a two-dimensional finite difference code that calculates the effects of impulsive loading of solid media for underground and cratering applications. It is more complex than a code limited to hydrodynamics in that it considers the tensor stresses associated with a solid material failure,

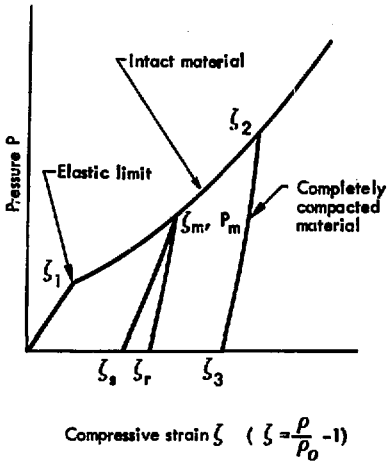

Fig. 1. P-ζ diagram showing compaction effects as applied in TENSOR74.

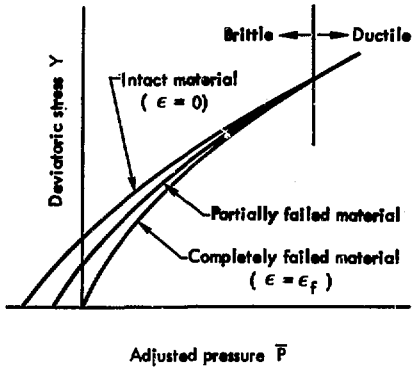

Fig. 2. Y-$\bar{P}$ diagram showing failure envelopes as applied in TENSOR74.

where highly nonlinear effects are encountered.

Two different types of inelastic behavoir are provided for in the TENSOR74 code, the first being a simple compaction of the medium. When the medium is subjected to a pressure beyond its elastic limit, the material undergoes permanent compaction and unloads along a path that lies below the loading curve in a plot of pressure against volume, as shown in Fig. 1. The degree of compaction and the unloading path depend upon the degree of overload beyond the elastic limit up to a specified maximum pressure. Beyond this maximum pressure, it is assumed that all the inherent porosity has been removed from the material, and the loading and unloading curves coincide. This type of inelastic behavior results in an attenuation of the stress wave as it passes through the medium. A more detailed description of the failure treatment is given in Appendix A.

The second type of failure involves shearing motion or tensile breakage of the material, which is also described in Appendix A. Before failure, the material can sustain deviatoric (shear) stresses as specified by a Y-$\bar{P}$ failure curve for intact material. After failure, the limiting values of deviatoric stress are reduced, although they still exist. Failure curves for intact and for failed material are shown in Fig. 2. Even completely crushed material can sustain some shear stress (up to a fraction of the confining pressure).

When the stress state of the material first moves beyond the failure envelope, failure is assumed to occur, and the deviatoric stresses are relaxed down to the curve for failed material with a time constant supplied as input data for the calculation. Partial failure, where the stress state is relaxed to a failure curve lying between the curves for intact and completely failed material, is provided for.

The failure curves indicate that the material normally has higher shear strength at larger values of confining pressures. At very large values of confining pressures, the failure curves merge into a single curve at a point called the brittle-ductile transition. Beyond this point the peak shear stresses are absolutely limited by this curve, without a time delay for relaxation.

The experimental information on failure of most materials is incomplete, so we have made assumptions here in the numerical calculations. The validity of these assumptions can be checked by subsequent comparison of these calculational results with the results from field experiments in the appropriate media.

Constitutive Relations

The data on the rock medium required as input for the calculations include the initial density and elastic properties, volumetric compressibility of intact and fully-compacted rock, and shear strength as a function of confining pressure. This information is normally obtained from geophysical field measurements, laboratory compressibility and triaxial strength tests, high-pressure Hugoniot measurements, etc. Data have been accumulated for a broad spectrum of rock types, densities, and porosities. A method recently developed by T. R. Butkovich uses simple mixture theory to simulate the complete equation of state of a rock-water-air matrix.[19] This method, which requires only the rock grain density, porosity, water content, and initial (elastic) bulk modulus as input, reproduces the equations of state for a wide variety of silicate rocks.

The physical properties assumed for the sandstone medium are listed in Table 1. These parameters are representative of the densest and least porous sandstone formations encountered at the Trinidad and R. D. Bailey excavation sites (U.S. Army Corps of Engineers), for which extensive geophysical data are available.[20-22] These data have been used in conjunction with the modified Butkovich technique to generate equations of state. In each case, the compression ζ as a function of pressure* and the shear strength as a function of confining pressure are determined. The compressibility curves are shown in Fig. 3, giving the initial loading behavior and the release path for fully compacted rock (all air voids removed, release from very high pressure). These two curves are quite close together, indicating that the sandstone has low porosity. This leads to a relatively small amount of compaction, so that the resulting stress-wave attenuation should be small. The shear strength as a function of mean-confining pressure is presented in Fig. 4 for intact and for completely fractured sandstone.

It has been proposed to use buffer zones of rock previously fractured by

*Compression ζ is defined as

$$\zeta = \frac{V_o}{V} - 1,$$

where V_o = initial specific volume of the rock matrix at zero pressure,
and V = specific volume at a pressure P.

Table 1. Physical properties of the sandstone and crushed sand media.

Medium	Bulk density ρ_0(g/cm^3)	Grain density ρ_g(g/cm^3)	Water content by weight	Degree of saturation	Total porosity	Initial bulk modulus k(kb)	Sonic velocity V_s (m/s)	Poisson's ratio ν	Tensile strength (bar)
Sandstone	2.5417	2.68	0.0125	0.50	0.0634	97.2	2652	0.24[b]	≈40
Crushed bulked sandstone	2.0354[a]	2.68	0.0125	0.1016	0.25	40.8	1880	0.3[b]	0

[a]Bulked by approximately 25% relative to intact sandstone material.

[b]Constant Poisson's ratio for each material is assumed in these calculations.

small-charge detonations in the controlled blasting design. The scope of this study includes calculation of the shock attenuation by broken and bulked material in the buffer zone. Therefore, an additional description is required to characterize this material. Buffer zone properties in practical applications would be expected to vary considerably with depth and emplacement design. It is probably most important to control overbreak near the surface, and in this region the buffer zone material should be bulked and relatively porous. For this reason, the sandstone described

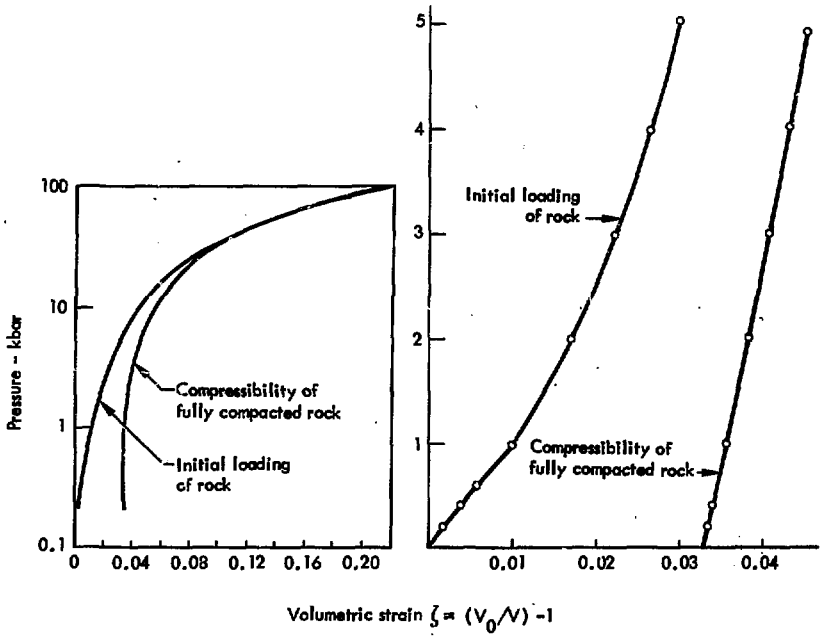

Fig. 3. Compressibility of sandstone.

previously has been bulked or decreased in density by about 25% to simulate the crushed buffer region. Grain density and water content are unchanged. These assumptions produce a material of porosity approximately midway between the intact sandstone and fine-grained sand. The physical properties of this crushed material are listed in Table 1, and the compressibility and shear strength curves are presented in Figs. 5 and 6. The greater initial air void porosity is evident in Fig. 5 from a comparison of the initial loading and fully-compacted compressibility curves. Since the material is assumed to be crushed and broken, it has no tensile strength.

Explosive properties of interest include the initial density, detonation velocity, energy release, Chapman-Jouguet point, and the expansion adiabat of the gaseous products. These properties may be formulated in terms of the Jones-Wilkins-Lee (JWL) equation of state.[23] The JWL parameters are calculated from experimental data on the detonation of metal-encased explosive spheres and cylinders. These data have been obtained for a gelled nitromethane and for an ammonium nitrate fuel oil (ANFO); their values are given in Table 2.[24-27] These explosives contained special-purpose additives for this project, so the data are not entirely correct for more conventional forms of these explosives.

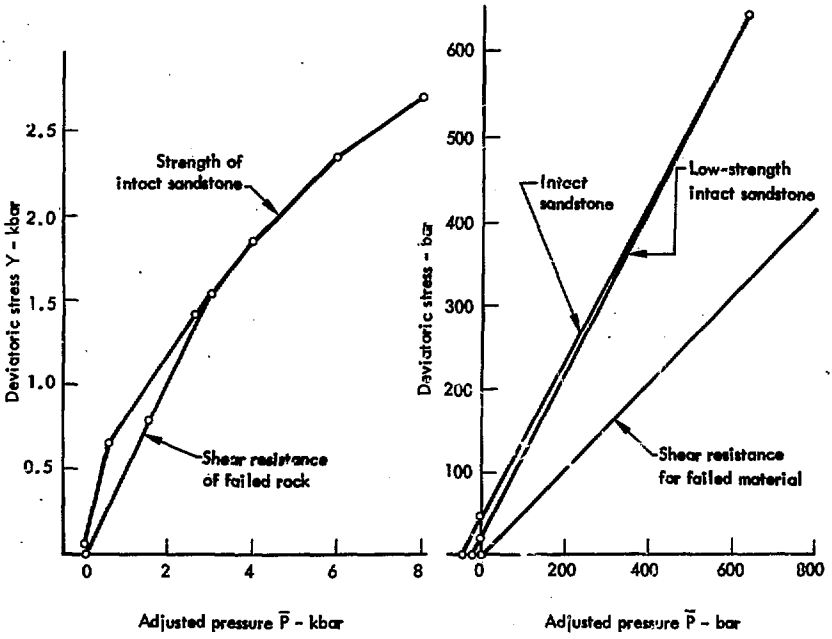

Fig. 4. Shear strength of sandstone.

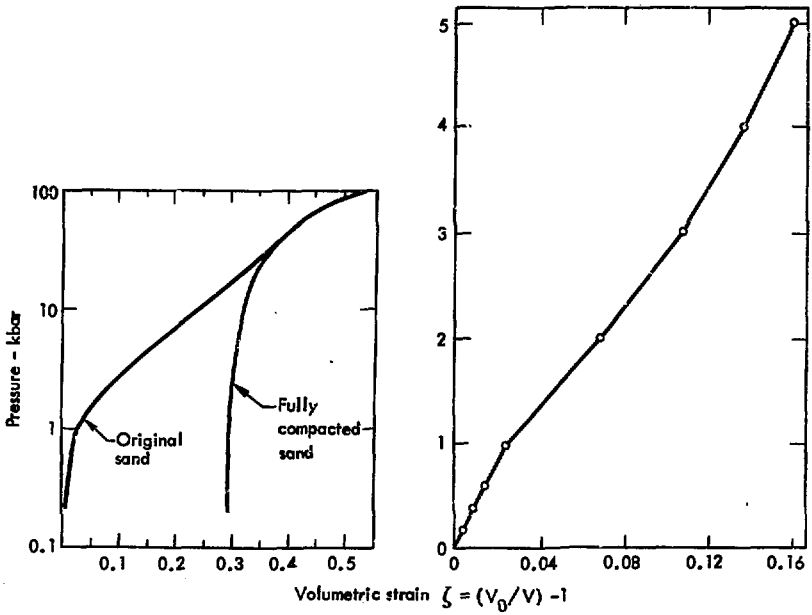

Fig. 5. Compressibility of material used in buffer zones.

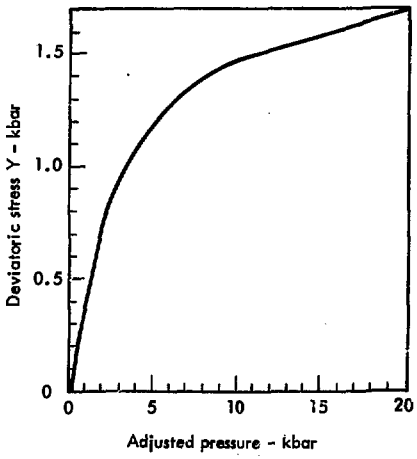

Fig. 6. Shear strength of material used in buffer zones.

Table 2. Physical properties and Jones-Wilkins-Lee (JWL) coefficients[a] for nitromethane and ANFO explosives.

Explosive	Gelled nitromethane[b]	Ammonium nitrate fuel oil (ANFO)
Bulk density ρ_0(g/cm^3)	1.21	0.782
Detonation velocity (m/s)	6,210	5,000
Total energy release (Mb-cm^3/cm^3)	0.045	0.029
Chapman-Jouguet pressure (kb)	120	50
Chapman-Jouguet compression ζ_{cj}	0.34614	0.34364
R_1	4.9	4.3
A_1 (Mbar)	3.180	1.02987
B_i (Mbar)	0.06378	-0.00574
W_1	0.38	0.28
R_2	1.4	1.2

[a]The JWL equation of state has been developed to describe the pressure-volume-energy behavior of high-explosive detonation products, as observed in metal acceleration experiments. Application of the JWL equation of state requires a knowledge of the bulk density, detonation velocity, total energy release, and Chapman-Jouguet compression of the explosive, plus the JWL coefficients for the following equation:

$$P = A_1\left(1 - \frac{W_1}{R_1\, V/V_0}\right)e^{-R_1\, V/V_0} + B_1\left(1 - \frac{W_1}{R_2\, V/V_0}\right)e^{-R_2\, V/V_0} + \frac{W_1 E}{V/V_0},$$

where P = Pressure (Mb), E = Energy content (Mb-cm^3/cm^3), V/V_0 = Specific volume of detonation products per initial specific volume of explosive.

[b]The nitromethane equation of state was derived for a special formulation of gelled nitromethane with particulate sand inclusions; this explosive was used during field tests of the Project ESSEX program.

TENSOR74 Calculations

The controlled blasting configuration on which the rock response calculations were made is shown in Fig. 7a. This included a vertical cylinder of explosive 12.7 cm (5 in.) in diameter and 490 cm (16.08 ft) long, with the top 270 cm (8.86 ft) below the surface of the ground. The length-to-diameter ratio is nearly forty for this configuration. The resulting volume of explosive was 6.2×10^4 cm^3. When gelled nitromethane was used as the explosive, this gave a weight of

75.1 kg (165.6 lb) with an energy release of 2.79×10^8 J. When ANFO was used, the resulting weight was 48.5 kg (107.0 lb) with an energy content of 1.80×10^8 J.

In the basic reference problem or standard configuration, the explosive used was a gelled nitromethane, initiated at the bottom, in a uniform sandstone medium. Comparative runs were made to give information on the effect of the variations in the configuration and in the material properties, as listed here:

Run 1. The tensile strength of the sandstone was reduced.

Run 2. The nitromethane explosive was replaced by the slower-burning less-dense ANFO.

Run 3. The explosive was initiated at the top of the cylinder rather than at the bottom.

Run 4. A slip surface was included.

Run 5. A buffer zone was included.

Run 6. A buffer zone and a slip surface were included.

All calculations were made in a two-dimensional cylindrical geometry, with the axis of the explosive column located at the axis of symmetry of the coordinate system. In the diagrams of Fig. 7 and almost all of the following figures, the explosive was located along the left edge, at r = 0, and extended from z-coordinate 840 cm up to 1330 cm. The rock surface was located at 1600 cm. This grid was

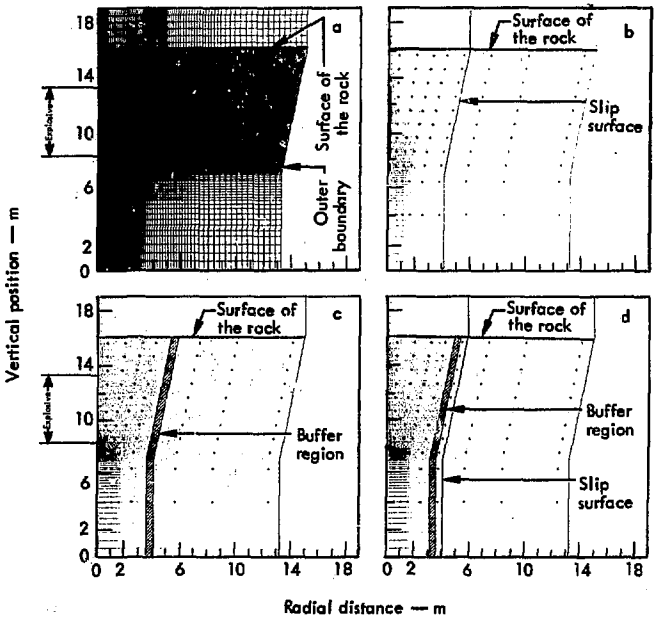

Fig. 7. Zoning of controlled blasting configurations.

made large enough so that the ground interaction of interest near the explosive would have been completed before any reflected wave could arrive from the finite outer-grid boundaries. The zoning was relatively fine near the explosive energy source, where good detail in the calculations was desired, and the zone size was gradually increased beyond the central region so that a large region could be covered to delay the arrival of boundary reflections without adding too many zones. The resulting mesh was 82 by 108 zones in size, with zone size ranging from 6.5 cm in minimum dimension near the explosive to 40 cm in maximum dimension near the outer boundaries. The rock included was 16 m in depth and extended to a horizontal range of roughly 14 m. In this zoning, the explosive cylinder was only one zone wide but 49 zones long because of the proportions of the cylinder.

In the TENSOR74 code, the geometry of a problem is specified with a roughly orthogonal set of K and L lines, forming the grid as shown in Fig. 7. The K-lines were oriented vertically near the charge, but were given a slope of up to 1:5 further from the axis. In the code, any K-line may be specified a slip surface as shown in Figs. 5b and d. The code does not permit a slip surface to terminate at a free surface, so that low-density resilient material was added above the surface of the rock to allow for the inclusion of the free surface and the intersecting slip surface at the same time.

The shock velocity in the sandstone medium was close to or somewhat greater than 2650 m/s (the sonic velocity) which led to calculational time steps of the order of 3 μs per cycle. For a problem length of 6 ms, approximately 90 min of computer time was required to complete a single problem on a CDC 7600 computer.

The relaxation time constant used for rock failure was set at 20 μs. The shock or dilatational strain-damping parameter was set to give a characteristic shock width of 100 cm. The multiplying factor for the deviatoric damping with respect to the dilatational strain damping was set at unity.

Compressional Waves

In the standard problem, the explosive is initiated at the lower end of the cylinder and produces an outgoing pressure wave, as shown in Fig. 8. These figures of the pressure contours, and most of the following figures, have been obtained directly from the TENPLT routine. The explosive detonation velocity is higher than the sonic velocity of the compressional wave through the sandstone, so the compressional wavefront takes a conical form during the burn of the explosive (somewhat less than 1 ms). After this time, the stress wave tends to become more spherical in shape. The early history of the stress waves in the rock medium is discussed in greater detail in later sections of this report. At early times the source region is all at high pressure, but at later times an outgoing wave is observed with residual pressures remaining behind the wave. The peak pressures at angles above the horizontal are higher than those below the

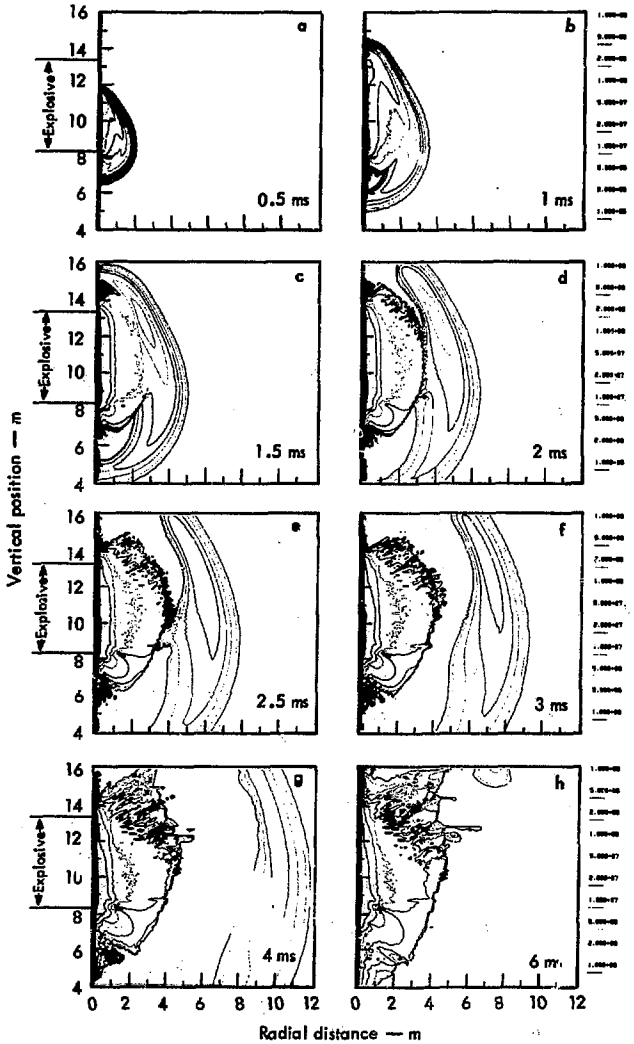

Fig. 8. Outgoing pressure wave in uniform medium.

horizontal because in the diagonally upward direction the pressure contributions from the various points along the explosive stick tend to arrive at the same time, while in the downward directions these contributions are spread out in time. The plots of negative pressure in Fig. 9 indicate that the outgoing compressional phase of the shock wave is followed by a tensile phase. This tensile phase develops most rapidly in regions of divergent expansion of the shock from the ends of the explosive stock, but is suppressed strongly in the horizontal direction from the side of the explosive. The tensile phase amplitudes are limited by the tensile strength of the medium. When larger tensile stresses are imposed, the medium fails and the tensile stresses are relaxed.

The TENPLT results for the pressures and for other parameters presented in this report are in general agreement with the results of photoelastic experiments performed by Dally, Fourney, and Holloway at the University of Maryland.[28,29]

The motion of the pressure wave is obscured to some extent by the residual pressures remaining in the medium. Another indicator of the wave propagation is the rate of strain of the zones in the calculations. In the TENPLT output this

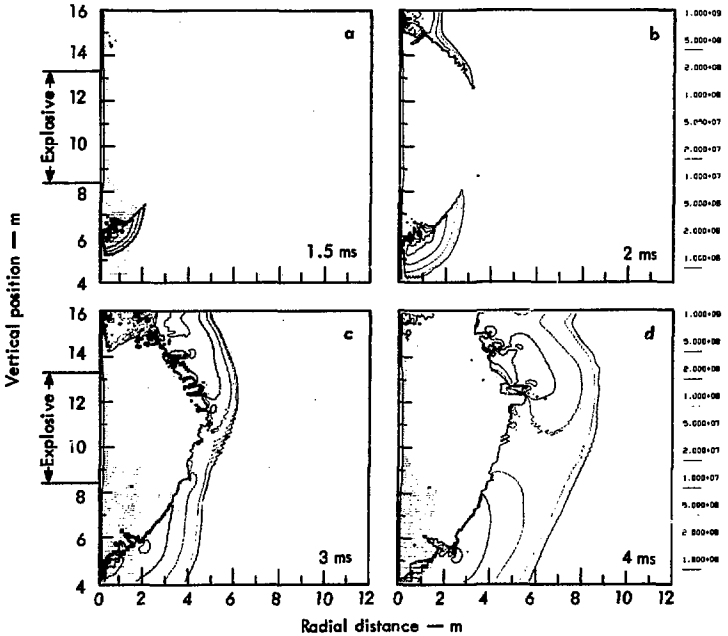

Fig. 9. Negative pressure plots in uniform medium.

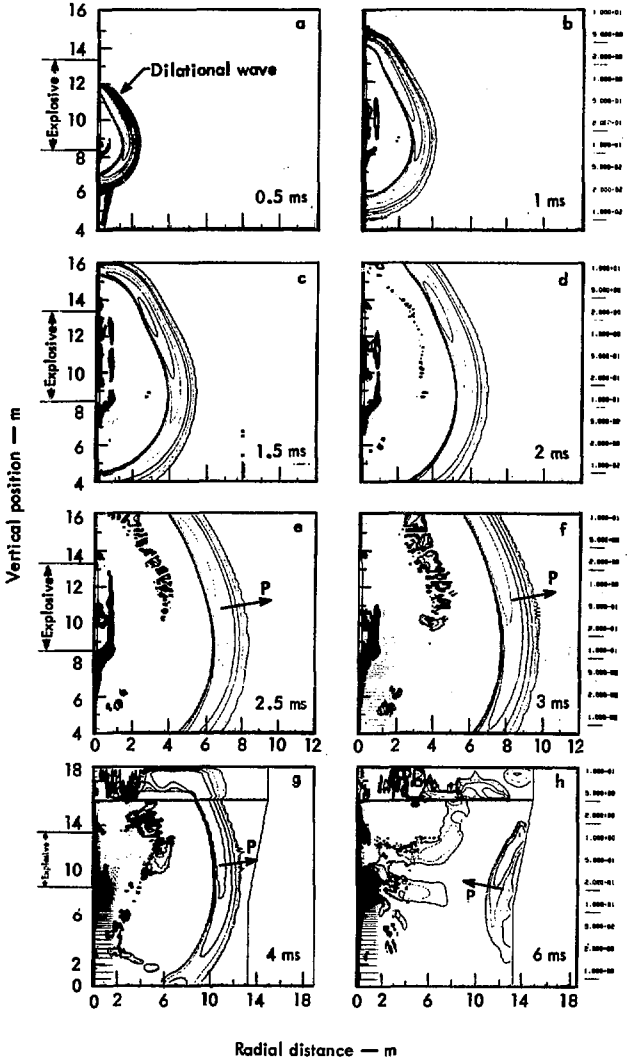

Fig. 10. Compressional phase of dilatational strain wave (DIVV NEG) in uniform medium. The sizes of the area in g and h are enlarged to show the interaction of the dilatational wave with the rigid outer boundary.

has been denoted as DIVV (the divergence of the velocity), where DIVV = $\frac{1}{V}\frac{dV}{dt}$, V being the volume of the particular zone. Since the positive divergence of the velocity represents an expansion rather than a compression, the negative divergence represents a compressional wave. This negative divergence function was obtained in the TENPLT routine by multiplying all the values for divergence by minus one. This converted large negative values into large positive values in the graphical output. Plots of the negative divergence of the velocity are shown in Fig. 10, where the compressional phase of the outgoing shock has been clearly isolated. Figure 11 presents the positive divergence or expansion phase, which is less sharply localized in space.

A broadening of the stress wave as it moves outward, which is caused by the artificial viscosity or shock-damping parameter added to stabilize the calculations and by the effects of compaction and of failure, is observed. The larger zones used in the outer part of the grid also contribute to broadening the stress wave through decreased spatial resolution. Viecelli[30] recommends using 20 mesh points per shock wavelength; the number here at large radii is considerably smaller for the practical reasons of

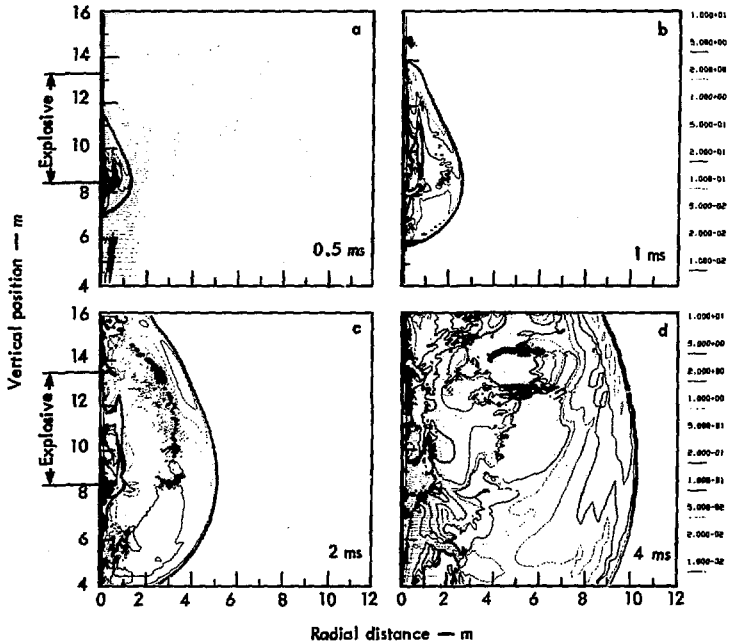

Fig. 11. Expansion phase of dilatational strain wave (DIVV) in uniform medium.

computer storage and running-time limitation.

Apparently random noise appears in the low pressure and tensile region well behind the front. This noise is not directly related to dilatational shock damping but is caused by tensile failure in the medium. The expanding zones undergoing tensile failure appear as regions of large positive devergence. The zones between the current tensile failure locations, being released from tension, appear as regions of negative divergence.

Shear Waves

GENERAL DISCUSSION

The two general types of body waves in uniform materials are dilatational and shear waves. The dilatational waves are the compressive waves discussed up to this point, in which a change in volume of the zones occurs as the wave passes. The particle motion is back and forth in the direction of wave propagation. Transient shear forces are created by the wave passage, but only because of the one-dimensional strain imposed on the volume elements of the medium during wave passage. The planes of shear maxima lie at 45 degrees from the direction of advance of the dilatational waves.

In shear waves, there are no compressive forces and no changes in volume during wave passage. Both the maximum shear stresses and the particle motions are at right angles to the direction of shear wave propagation.

In a uniform, linearly elastic medium, the dynamic equations of elasticity can be divided into two parts; one involving the scalar potential, from which solutions for the dilatational waves can be obtained, and the other involving the vector potential, from which the shear wave solutions can be obtained. These two fields are completely uncoupled from each other except at the boundaries, so that each type of wave in the interior of the medium should behave as if the other type were not there. Coupling will occur when the stress-strain curve for the medium becomes nonlinear or when the deformations become too large. A mathematical analysis of this separation into the two types of fields is given in Appendix B.

Just as the dilatational waves could be isolated by finding the divergence of the velocity, the shear waves can be isolated by finding the curl of the velocity. Since the dilatational waves have zero curl and the shear waves have zero divergence, these two vector operations separate the two independent wave fields. The DIVV operation leads directly to the dilatational strain rate, $\dot{\theta}$, which can be regarded as the strain wave itself. The curl V operation gives the rotation of the elements, which in itself does not define the strain rate associated with shear waves. For instance, if the mesh were rotating uniformly, the curl V would be constant over the mesh and no shear waves would be present. When there is a variation in curl V, the gradient of the curl vector involves shear-strain rates and shear waves. Since there is no uniform

rotation imposed on the whole mesh here, the curl V quantity will be considered to indicate the presence of the shear wave directly.

SHEAR WAVE GENERATION

In a spherically symmetric explosion in an infinite medium, no shear waves should be created at all. Shear waves are created by asymmetric or shear forces at the source, by stress-wave reflections at the surface, and through interactions at media interfaces or discontinuities. In this particular problem, the explosive stick is separated from the rock medium by a slip surface, across which no shear forces can be transmitted; however, a shear wave is generated at the rock-explosive interface because of the progressive burn of the explosive.

If the entire explosive cylinder is initiated simultaneously, the outgoing dilatational wave is initially cylindrical in form. The principal stress ellipsoid at some point in the cylindrical wave in the stressed rock is oriented with one axis in the r-direction, another in the z-direction, and a third in the ϕ-direction. The maxima of the associated shear stresses lie in directions that bisect the angles between the pairs of principal stresses. The shear stresses in the direction of the principal compressive-tensile stresses are zero. Consequently, the shear stress along the rock-explosive interface is zero in this case.

When the explosive is initiated at one end, the outgoing stress wave is conical in form rather than cylindrical. The principal stress ellipsoid for the point in the rock is tilted, with one principal stress lying in the direction of advance of the wave, normal to the conical wavefront. A second principal stress is oriented parallel to the wavefront and is in the r-z plane, and the third is in the ϕ-direction. The directions of the maxima and the nulls of the shear stress field are also rotated with respect to the cylindrical case so that a null of the shear stress field does not lie in the z-direction, parallel to the rock-explosive interface. Consequently, a shear-stress component must exist along this interface when the conical dilatational wave is initiated.

In physical reality, the shear stress that can be transmitted across the rock-explosive interface is small because of the low viscosity of the gas from the explosive. In the numerical calculations, no shear stress can be transmitted because of the pressure of the slip surface. Therefore, the shear-stress component existing in the dilatational wave must be cancelled by an opposite shear stress that initiates an outgoing shear wave. This shear wave must also have a conical form because of the moving point of initiation, but the angle is different because the velocity of the shear wave in the rock medium differs from that of the dilatational wave.

SHEAR WAVES AS CALCULATED BY TENSOR74

In the two-dimensional calculations, variations of zonal quantities occur only in the r and z directions; cylindrical symmetry is assumed and there is no ϕ component of velocity. Consequently, the curl V vector has components only in the ϕ direction. The coordinate system used in these calculations is right-handed in

the sequence of variables r, z, and ϕ, where z is positive upward and ϕ is positive out of the r-z plane of the paper so that a counterclockwise eddy in the velocity field gives a positive value for curl V.

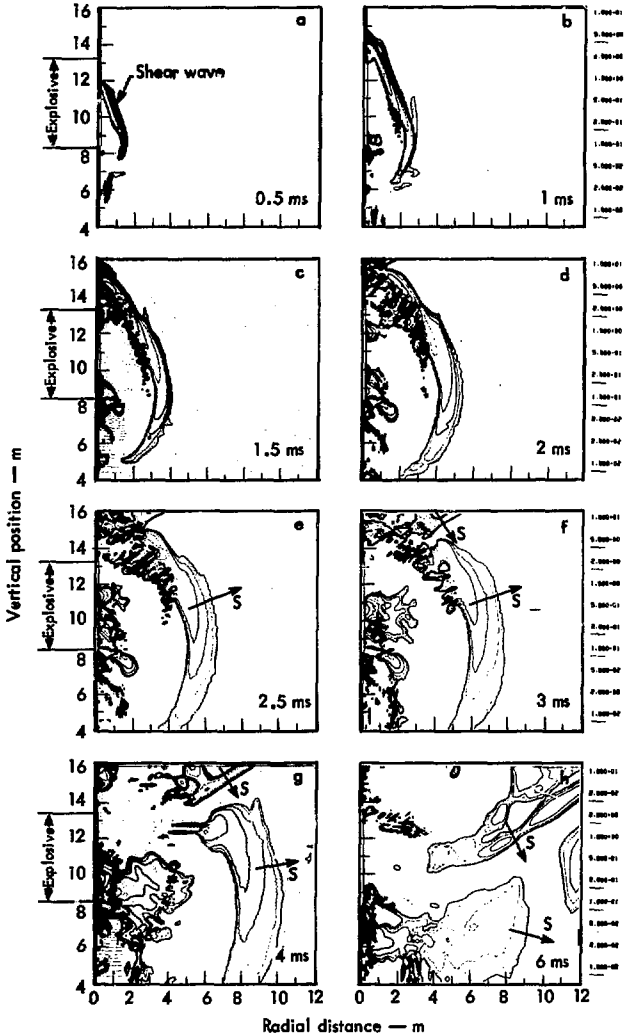

Fig. 12. Counterclockwise phase of shear wave (CURLV) in uniform medium.

TENSOR74 results for positive curl V are shown in Fig. 12 and for negative curl V in Fig. 13. At early times the conical form of the shear wave is evident, but after the completion of the explosive burn at about 1 ms the shear wave becomes less conical and more spherical in shape. At about 1.5 ms, the dilatational wave reaches the surface and a second shear wave is generated, with a polarity the reverse of the shear wave from the source. This wave moves downward with the shape of an inverted cone. At 4 ms, the leading part of this wave, with negative curl V, is contiguous with the secondary part of the shear wave from the source, which also has a negative curl V. The corresponding plot of positive curl V at 4 ms shows that the leading portion of the shear wave from the explosive and the secondary portion of the shear wave from the surface are separated from each other by an area of destructive interference.

An example of shear wave generation caused by the arrival of a dilatational wave at a discontinuity inside a medium is given by the calculational results of a slip surface, Fig. 14. When the outgoing compressive wave reaches the slip surface, both transmitted and reflected dilatational and shear waves should appear. The reflected compressional wave is not of

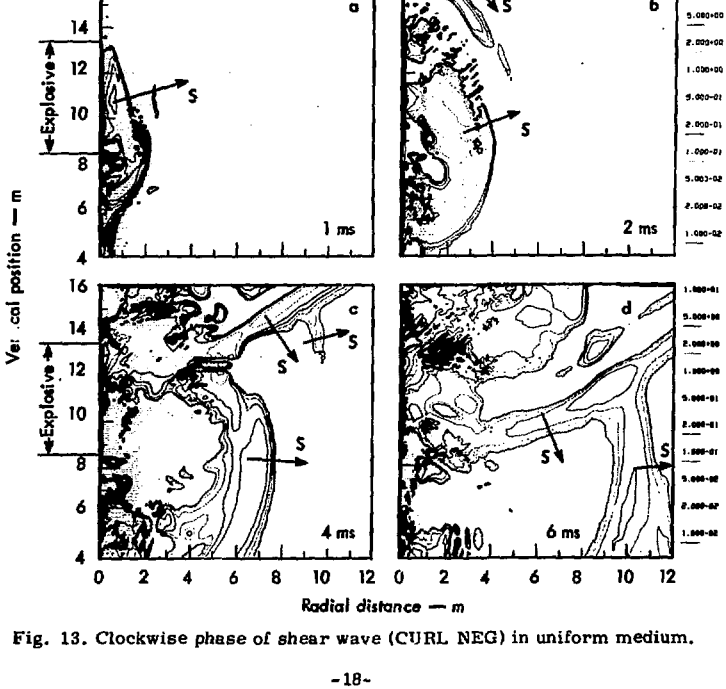

Fig. 13. Clockwise phase of shear wave (CURL NEG) in uniform medium.

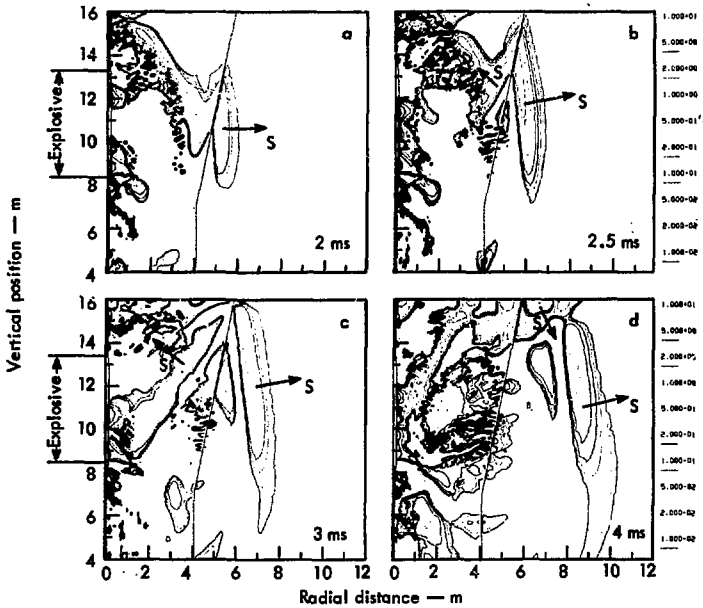

Fig. 14. Counterclockwise phase of shear wave (CURLV) with slip surface.

significant amplitude here, but the shear waves created are very obvious, radiating from a generation point following the crossing of the compressional wave with the slip surface and moving outward from the surface in both directions. The shear wave moving back from the slip plane encounters the region of irregularly failed material and residual motions, but is still visible at 4 ms, Fig. 14d. The shear wave moving in the direction of increasing radial distance maintains its form as it moves through the unfailed material. The shear wave created by the arrival of the dilatational wave at the upper boundary has begun to move downward and to merge with the slip-surface shear wave at 4 ms, Fig. 14d.

Velocities

PARTICLE VELOCITY

Further information on rock blasting phenomena can be obtained from a study of particle and wave velocities. The particle velocities are obtainable directly from the TENPLT plots, while the wave velocities must be deduced from other

output data. The directions of the particle motions at successive times for the case of the explosion in the uniform medium is given in Fig. 15, where the lengths of the vectors do not have significance. Alternate plots, where the lengths are proportional to the velocities, are given in Fig. 16 (several different scales were used). These plots show the early simple expansion, primarily indicating an outgoing dilatational wave, and the later more complicated velocity patterns, including counterclockwise and clockwise velocity eddies that can be identified on the curl V and negative curl V plots of Figs. 12 and 13.

An interesting and significant series of velocity plots where a slip surface is present is shown in Fig. 17. At earlier times there does not seem to be an appreciable effect from the slip surface, but at later times the particle motion within the surface has been directed upward, and the particle motion outside the surface has subsided to a relatively low value. This indicates that the slip surface is very effective in redirecting the outgoing radial motion into a more vertical direction.

STRESS WAVE VELOCITY

The sonic velocity of a dilatation wave is given by the relation

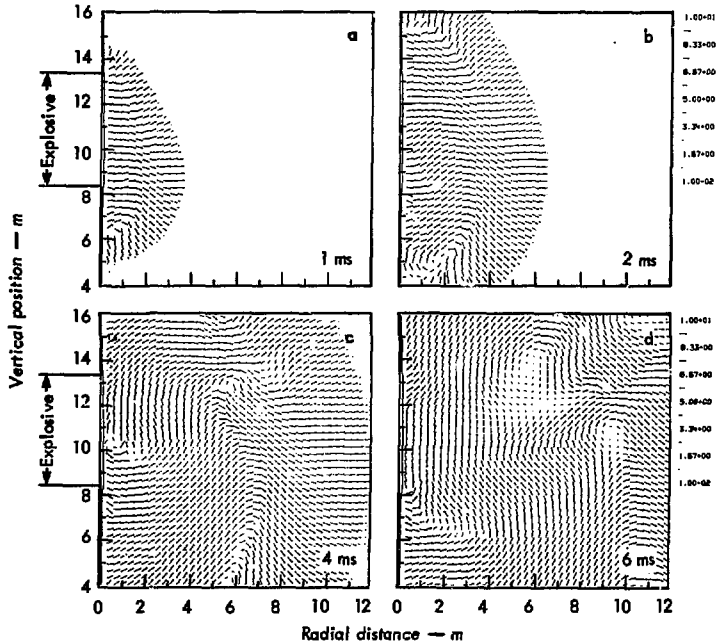

Fig. 15. Direction of particle motion in uniform medium.

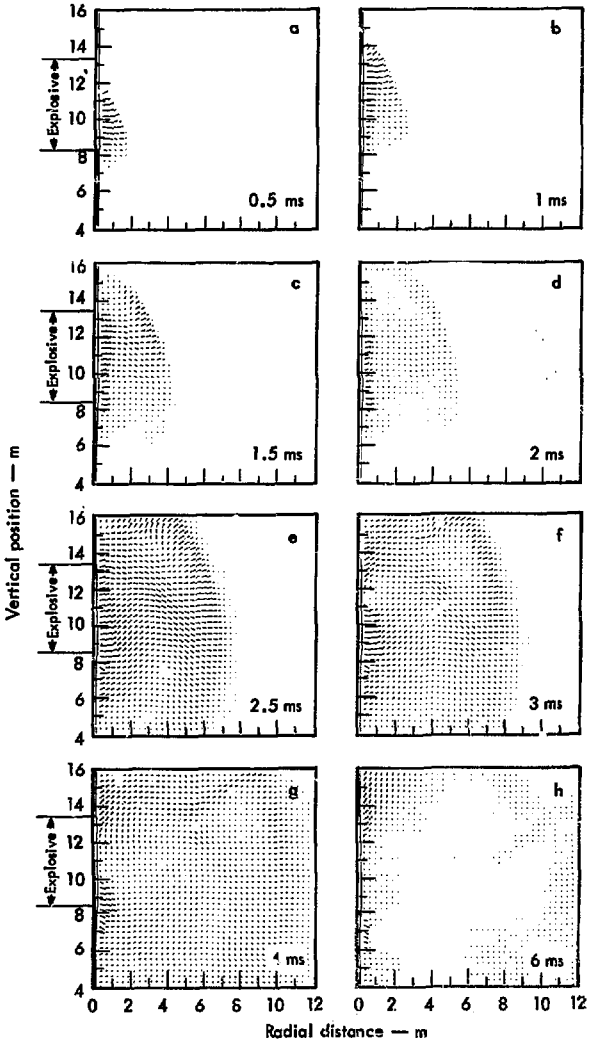

Fig. 16. Amplitude and direction of particle motion in uniform medium.

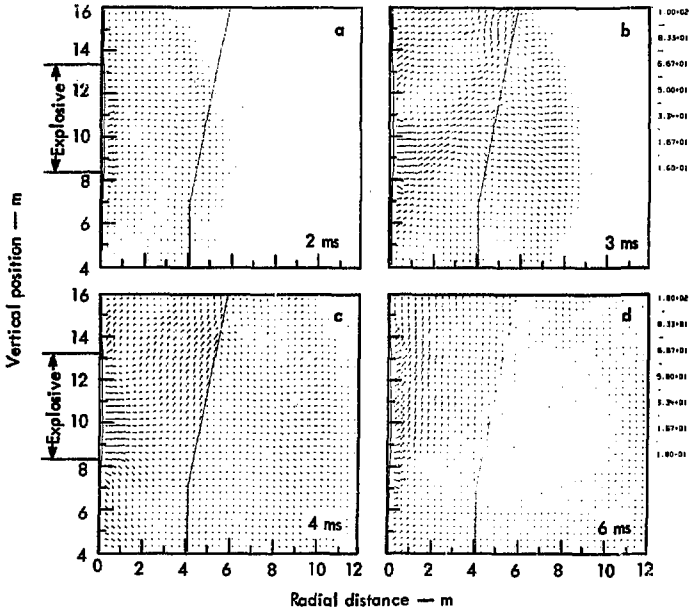

Fig. 17. Amplitude and direction of particle motion with slip surface.

$$V_c = \left[\left(K + \frac{4\mu}{3}\right)/\rho\right]^{1/2} ,$$

where ρ is density, K is bulk modulus, and μ is shear modulus; μ is related to bulk modulus and Poisson's ratio ν by the formula

$$\mu = \frac{2(1 - 2\nu)K}{2(\nu + 1)} .$$

The sonic velocity of a shear wave is given by

$$V_s = [\mu/\rho]^{1/2} .$$

From these formulae, the sonic velocities in the sandstone are 2650 m/s for the dilatational waves and 1550 m/s for the shear waves.

Measurements on the progress of the calculated dilatational wave as shown in Fig. 10 indicate that up to about 1 ms the average dilatational wave velocity was about 3000 m/s, and from 1 to 3 ms it was about 2600 m/s. Because of the shape of the P-ξ curve the larger amplitude compressional waves have a larger bulk modulus and should move at a higher velocity than the lower amplitude ones, so it is concluded that the calculations give satisfactory values for these velocities.

Corresponding measurements on the shear wave as shown in Fig. 12 give

rather high shear-wave velocities; for velocities between 1 and 2 ms, about 2000 m/s are indicated. At ranges close to the explosive, intense failure gives rise to nonlinear behavior of the medium. There is a continuous transfer of energy from the dilatational wave to the shear wave, resulting in an apparent higher velocity for the shear wave. It is noted that in the linear elastic case, the velocities of the shear waves should be independent of their amplitudes because the shear modulus is directly related only to the bulk modulus and to a constant Poisson's ratio. This bulk modulus is directly related to the slope of the P-ξ curve at the particular pressure in that zone, but the passing shear wave does not raise the pressure. There are differing pressures throughout the grid, however, and this will lead to some variation in the shear velocity.

ANGLE OF WAVEFRONTS

Another indicator of wave velocity is the angle of the conical wavefront emerging from the explosive source. The angle between the wave propagation direction and the explosive column is given by the relation

$$\sin \theta = V_s/V_e ,$$

where V_s is the wave velocity in the sandstone medium and V_e is the detonation velocity of the explosive. Comparisons between calculated values and the angles measured on the TENSOR output contours have been made for the problems where the explosive was nitromethane, with a detonation velocity of 6210 m/s, and for an ANFO explosive with a velocity of 5000 m/s. The angles were measured on the negative DIVV and the curl V plots of Figs. 10b and 12b for nitromethane at 1 ms, and in the corresponding plots for ANFO. The results of this comparison are given in Table 3. It is seen that when the angles are measured from the trailing edge of the first phase of the stress wave, where the wave is changing sign, the calculational results agree with those predicted for low-amplitude waves in the elastic regime.

Table 3. Predicted and measured angles of wavefronts of dilatational and shear waves at 1.0 ms.

	Nitromethane	ANFO
Detonation velocity V_e (m/s)	6210	5000
Dilatational sonic velocity V_d in sandstone (m/s)	2650	2650
Predicted angle from normal (= arcsin V_d/V_e)	25°	32°
Angle measured from TENSOR74 results	26°	32°
Shear wave sonic velocity V_s in sandstone (m/s)	1550	1550
Predicted angle from normal	14.5°	18°
Angle measured from TENSOR74 results	17°	19.5°

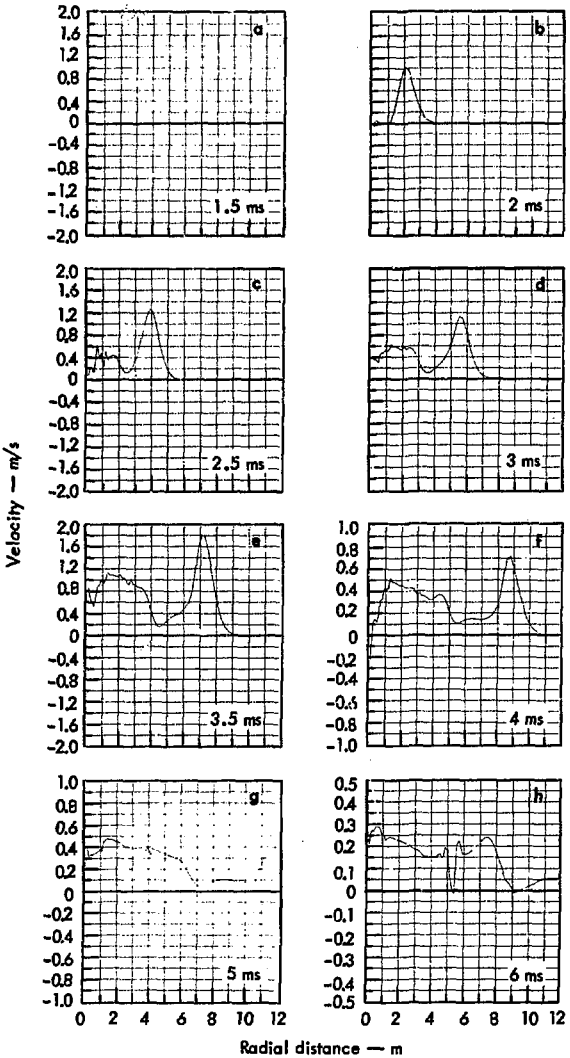

Fig. 18. Horizontal component of surface velocity in uniform medium.

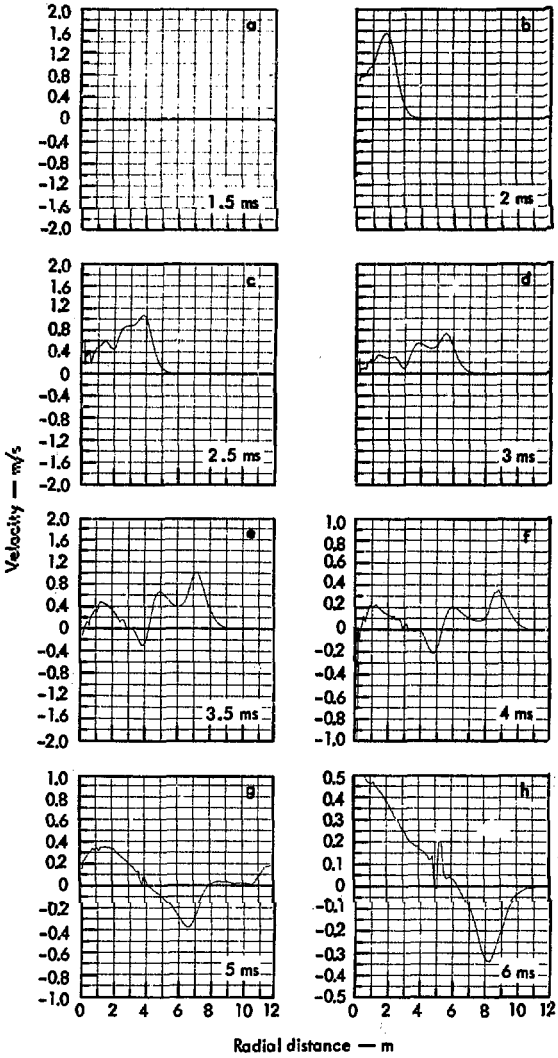

Fig. 19. Vertical component of surface velocity in uniform medium.

These velocity determinations are made at an earlier time than those described in the preceding section. The stress waves tend to broaden as they move outward because of the damping parameters and the stress relaxation effect included in the calculations. Consequently, the angles with the axis become somewhat indeterminate at late times.

SURFACE VELOCITY

Results from computer calculations on the surface velocity are useful because the vertical and horizontal components of velocity at the surface, or at other points within the medium, are variables that can be measured directly and inexpensively in the field with velocity gauges that check the computer results. Figures 18 and 19 show the computed horizontal and vertical components of velocity at the surface. These plots show the passage of the stress waves and the subsequent general motion of the surface.

It should be noted that Figs. 18 and 19, as well as the other graphical plots presented here, show the dependent variable (velocity) as a function of spatial location at a given time. Plots of the dependent variable as a function of time at a given location are, in general, not available because of storage space limitations. Values of the zonal quantities calculated for each cycle overwrite those quantities for the previous cycle, and these quantities are printed out or recorded for subsequent TENPLT processing only for a limited number of times during the problem history. The option of more complete output of a dependent variable as a function of time is available in TENSOR74 at the cost of the larger storage space required.

Material Failure

FAILURE CRITERIA

When a zone in the sandstone medium is dynamically loaded by the stress wave, the pressure and compression variables follow the sandstone P-ξ curve, and at the same time a corresponding path on the Y-$\bar{P}$ plot is traced out by the deviatoric stress variable Y and the modified pressure $\bar{P}$. These quantities Y and $\bar{P}$ are defined in Appendix C. When the deviatoric stresses become too large, the material fails, thus relaxing these deviatoric stresses. This failure point is dependent upon the pressure, so that the failure limit can be represented as a curve or surface in the Y-$\bar{P}$ space. A measure of rock failure or breaking is thus given by whether this path on the Y-$\bar{P}$ plane has crossed the failure surface. When failure of a zone occurs, this information is stored in the data ensemble for that particular zone, and can be retrieved later as the state variable, which takes on the values of elastic (unfailed) or cracking (undergoing failure).

The state plots at several times are given in Fig. 20. The contour of failure lags behind the front of the pressure wave because rock is very strong with respect to shear failure when under high hydrostatic pressure, but much weaker when

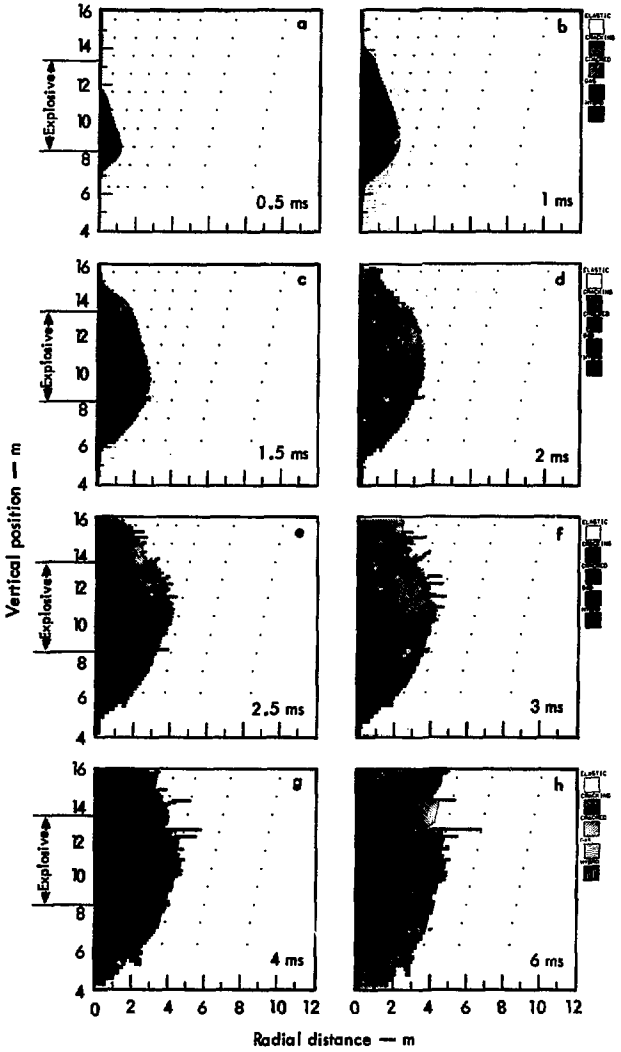

Fig. 20. State of the material in uniform medium.

pressure is removed. The tensile strength is relatively low.

The failure contour on state plots follows behind the shock out to about 1 ms, and state plots do not change appreciably after about 3 ms. The failure pattern at 6 ms can be taken as the final shape for predicting rock breakage in this controlled blasting application. The rock failure pattern very close to the axis is invalid because of the necessity of using a slip surface at the grid line between the explosive and the rock medium. Consequently, in the calculations some energy is directed preferentially upward and downward from the explosive, but the total energy involved here is not large.

A disadvantage with the use of the state parameter as a failure indicator is that it does not show degrees of failure. Rock zones that have just touched the failure envelope should retain a high degree of coherence, while those that have failed more completely should accordingly be reduced in strength to a greater degree. The failure model of TENSOR74 takes this degree of damage into account by storing for each zone a quantity SV1, the cumulative failure shear strain. This quantity represents the inelastic strain that the zone has undergone during failure as described in Appendix A, and is thus a measure of the damage to the rock medium. The material strength is progressively reduced to the lower completely failed envelope as the damage parameter approaches some prescribed value, one percent in these calculations. Figure 21 shows this quantity SV1 at various times in the progress of the problem. The lowest strain contour agrees closely with the failure contour of the state plots, but with this SV1 parameter additional contours of higher strain are also given within the low-strain contour.

Those definitions of rock failure are used to give internally consistent calculational procedures, but do not give quantitative descriptions of failure from an engineering point of view. Some work has been done on relating calculational degree of failure of granite to engineering properties.[31] In general, experimental investigations must be made on a rock such as the sandstone considered here, to translate the quantitative calculational state of the medium to engineering criteria, such as whether the failed rock can be shoveled out.

Another useful parameter is the maximum compressive strain. This quantity, denoted XMUS in the TENSOR74 output, is used in the calculations to show the degree of compaction that a zone has undergone so that the particular P-ζ relation to be used for that zone at that time can be specified. Ordinarily, XMUS achieves its final value upon the passage of the compressive stress-wave peak; all subsequent compressive strains are smaller in amplitude. There is a one-to-one relation between XMUS and the peak compressive stress that the zone has undergone, as specified by the loading portion of the P-ζ table for the sandstone medium.

As described in a following section, XMUS can also be used as an indicator for failure in shear upon the passage of a high-amplitude compressive-stress wave. In this calculation with the sandstone medium, this type of failure should occur only near the explosive.

The maximum compressive strains computed in this reference problem are

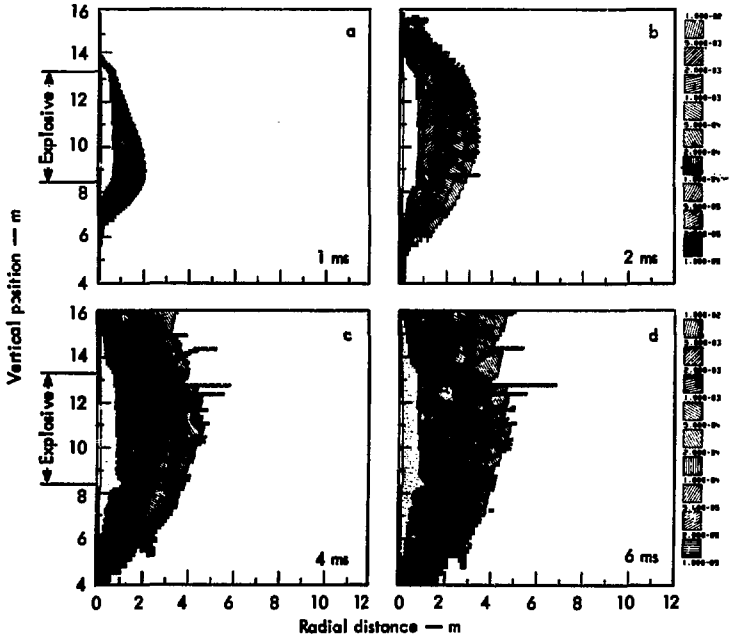

Fig. 21. Total inelastic strain (SV1) in uniform medium.

shown in Fig. 22. An interesting feature is the upward directivity or cone shape of the peak-strain contours; this phenomenon corresponds to the upward directivity of the pressure contours at the shock front as noted in the pressure plots of Fig. 6. The upward directivity tends to disappear and the peak-strain contours become more nearly spherical far from the source, as is shown in Fig. 22d at 6 ms.

Another quantity that may be regarded as a failure indicator from an engineering point of view, is the vector velocity. The velocity plots of Fig. 16 do not give an obvious indication of failure, but when a slip surface is added, as shown in Fig. 17, there is a strong velocity discontinuity across the surface, as noted earlier. In these plots, the entire cone within the slip surface may be regarded as failed and in the process of ejection.

RADIAL CRACKS

An important feature of rock mechanics is the type of cracking that arises through the unstable mechanics involved in the formation of a crack. When a crack is initiated, the stresses in regions adjacent to the crack plane are relaxed, but the stresses at the crack edges are magnified and concentrated. Consequently, the

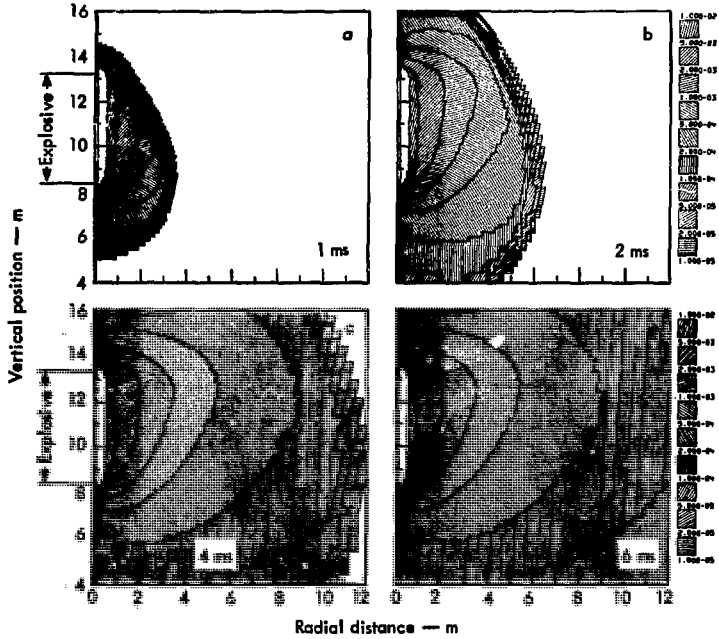

Fig. 22. Maximum compressional strain (XMUS) in uniform medium.

occurrence of a crack along some plane makes another nearby parallel crack less likely, while it increases the probability of failure of zones ahead of the crack. This phenomenon is common in the laboratory and in the field. In one-dimensional finite difference analysis, there is no way such cracks can appear because no azimuthal variation of parameters leading to azimuthal stress concentrations can occur. In the two-dimensional problem considered here, parameter variations can occur throughout the r-z grid, while in the ϕ direction the parameters are assumed to remain constant over the entire 360 degrees.

In this problem, the early expansion around the explosive source is mostly radial, creating tensile hoop stresses in the ϕ direction, but not in the r or z directions. Consequently, the early failure will be in planes with normals in the ϕ direction. Since the stress concentrations in the ϕ direction are not permitted, the material will fail in tension into uniformly failed material without initiation of localized cracks. In the version of TENSOR74 used here, the deviatoric stresses in the r and the z directions are relaxed at a slower rate than in the ϕ direction upon ϕ-stress failure, so that the possibility of creation

of a crack in the r-z mesh is increased. When the wave front has curvature in the r-z plane, the divergence of the material motion will lead to tensile stresses in this plane also; when this tension occurs in unfailed material, cracks may be initiated in planes with normals lying in the r-z plane. The stress concentrations at the crack edges will then cause these cracks to run ahead of the ϕ-stress failed material, and to grow radially as the medium expands radially. Cracks of this type will be called progressive cracks here.

This type of cracking behavior depends critically upon the concentration of tensile stress in a small area. In a finite difference calculation this localization of stress might occur in one or two zones. The usual practice in numerical calculations is to avoid such stress concentrations by spreading out stress variations over several zones to prevent spurious oscillations and to improve the accuracy of the finite difference procedures.[30] Further investigations must be made to satisfy these conflicting requirements. In addition, the actual effective tensile stress levels and time rates of failure for field materials are usually unknown. This indicates that the computer results must be normalized with the results from field tests.

This progressive cracking is significant in engineering applications since the volume covered by these cracks can be considered failed, even though in the regions between the cracks the medium may be completely intact. The size of these fragments should be directly dependent upon the spacing between the cracks, which in turn should be related to the stress history during tensile failure in that vicinity.[32] Further studies must be made to determine whether the TENSOR74 calculations do give realistic results for the spacing and the extent of these radial cracks.

It is probable that overbreak phenomena occurring in field applications are a manifestation of these random progressive cracks. The utility of presplit planes and buffer zones should lie in their ability to control and terminate these cracks.

The progressive failure cracks discussed here are evident in the late-time state plots of Fig. 20, and in the late SV1 plots of Fig. 21. The SV1 plots indicate that some of the regions were traversed by the progressive cracks at an earlier time and that overall failure occurred later.

The energy lost inelastically when these cracks are created is low because the tensile stresses are low and the stress change upon failure is small. The resulting failed material has thereby acquired a relatively small increment of internal energy in the form of additional surface. This contrasts with the case where shear failure occurs at the high-compressive stress associated with the passage of the stress wave. The absolute amount of shear-stress relaxation is then probably large, resulting in a large amount of new surface area, many dislocations and microfractures, and temperature rise of the medium.

In a dilatational wave, the leading compressional phase is usually followed by a rarefaction. The tensile failure that may occur from this rarefaction should result in cracks with planes parallel to the wave front. In this orientation and

with this transient state of tensile stress, these cracks should not progress outward. On the other hand, there are also transverse tensile stresses associated with a rarefaction, and if a radial crack already exists, the stress concentration effect acting on the transverse stress may lead to a growth of the existing radial cracks.

The computer results for this problem, as shown in Figs. 21b and c, indicate that this growth of radial cracks from the tensile phase of the stress wave is not occurring because the ends of these cracks are too far behind the outgoing stress wave. Instead, these progressive cracks are growing from the continuing radial expansion of the stressed region. The TENSOR74 program does not include the calculation of gas flow into the cracks, so that this calculated crack extension has not been caused by gas flow.

SPALL

Another phenomenon of practical importance is surface spalling, where the incident compressive stress wave reaches the surface and is reflected back into the medium as a tensile wave. As the tensile wave moves downward into the rock and cancels the decaying tail of the compressive wave, the net stress within the rock becomes tensile and rupture may occur. When rupture occurs, this tensile wave does not propagate deeper into the medium, and the rock spalls upward with reinforced vertical velocity.

The spalling behavior is not very evident in the negative pressure plots of Fig. 7 or the divergence plots of Fig. 9 because the failure seems to occur over a region several zones wide in these calculations, so that the spalling is not sharply defined. With shorter failure relaxation times and with smaller values of viscous damping, the calculated spalling would become more pronounced. A more concentrated energy source would also lead to more visible spalling. This spalling behavior is more evident in Figs. 23 and 24, giving the state and SV1 plots for a calculation with reduced tensile strength for the sandstone medium. In these figures, the rock failure near the surface appears to run ahead of the failure deeper into the medium, indicating the presence of the rarefaction wave returning from the surface.

FAILURE STUDY WITH Y-$\bar{P}$ PLOTS

A useful output from TENPLT is the graphical display of deviatoric stress Y versus adjusted pressure $\bar{P}$, as shown in Fig. 25. These points give the instantaneous Y-$\bar{P}$ variable states for the zones on plots showing the relation of these points to the failure surfaces and to loading and unloading lines.

On these plots, all the zones are originally at the state Y=0, $\bar{P}$=0. Upon the arrival of the dilatational stress wave, a zone undergoes a compression in the direction of the wave motion. If the width of the stress wave is small compared with the radial distance, the wave can be regarded as planar, with zero strain in the transverse directions. Under this condition, a linear relation will exist between Y and $\bar{P}$, with a slope of $1 - 2\nu$, where ν is Poisson's ratio, as is shown in Appendix C. The points will move up this line as the stress wave passes. For sufficiently intense plane waves, these

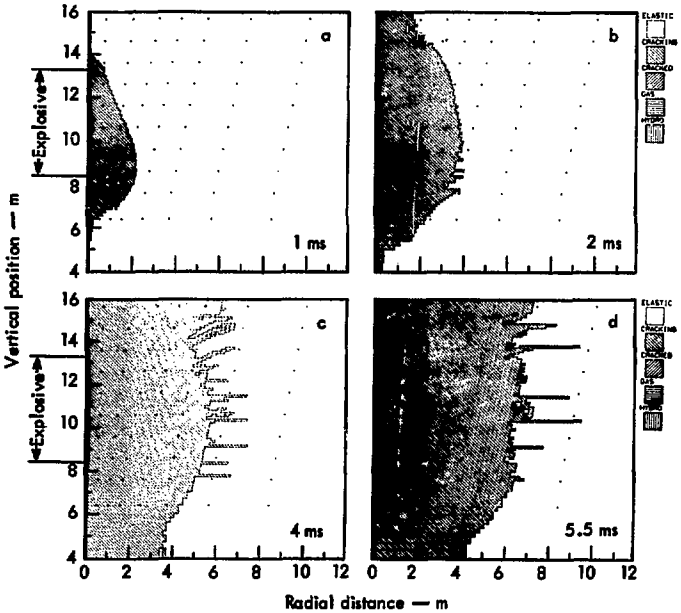

Fig. 23. Effect of lowered tensile strength on STATE.

points will reach and exceed the failure envelope for intact material, and the material in the corresponding zones will fail in compressive shear. The shear stresses will then be relaxed in the manner described in Appendix A, bringing these points below this failure surface for intact material.

There is a second failure surface on the Y-$\bar{P}$ plot, which represents the shear resistance for completely failed material. Zones that have undergone a very intense stress with an inelastic strain SV1 greater than 0.01 are classified as completely failed, and the deviatoric stresses are relaxed to this surface at a constant value of unadjusted pressure. Zones that have undergone less inelastic strain are classified as partially failed, and the deviatoric stresses are relaxed to failure surfaces intermediate between the surfaces for intact material and for completely crushed material, depending upon the value of inelastic strain SV1.

After the compressional-wave peak has passed, the unfailed Y-$\bar{P}$ points will move downward along this line of slope $1 - 2\nu$ again, while those that represent failed and relaxed zones will be displaced to positions below this line, and will then move downward with this same slope. The compaction of the medium will also affect the position of these points to some extent.

If the compressional wave is followed by a tensile phase, the points will move along the line of slope $1 - 2\nu$ down toward the origin of zero pressure and zero deviatoric stress. They will then move upward to the left with a negative slope of $1 - 2\nu$. Some of these points may reach tensile failure by this path, and the tensile stress will then be relaxed to zero, moving this point to the right again. In shear failure, only the deviatoric stress Y is relaxed, the unadjusted pressure remaining unchanged. In tensile failure, the tensile components of the stress tensor are relaxed, modifying both deviatoric stress and pressure.

The passage of the stress wave will impart an outward radial velocity to the medium. In addition, the gases from the explosive still exert an outward pressure gradient tending to move the medium outward. This motion relaxes the pressure in the gas and rock, but will add hoop stress to the deviatoric stress field. Consequently, during the passage of the stress wave the Y-$\bar{P}$ points will move up and down the line of slope $1 - 2\nu$, but with an additional displacement to the left of this line. This movement of the points will continue until the tensile stresses in the medium stop the radial motion, or until the points reach the failure surface

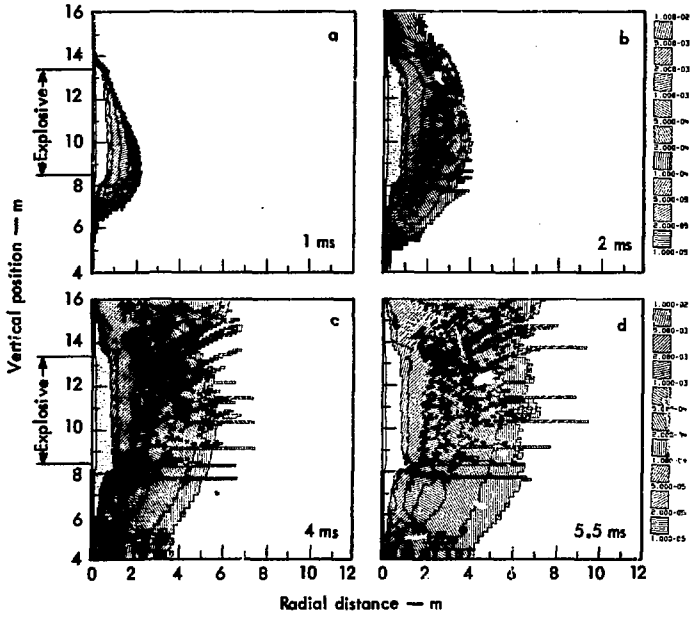

Fig. 24. Effect of lowered tensile strength on total inelastic strain (SV1).

and tensile failure occurs. Under tensile failure, the principal stress in tension is relaxed to zero with a time constant delay. As discussed in the section on radial cracks, these tensile hoop-stress cracks are geometrically different from the tensile cracks resulting from the tensile phase of the dilatational wave. They differ in that the hoop-stress cracks extend outward radially, while if the negative stress-wave cracks occur, they occur in onion-like layers.

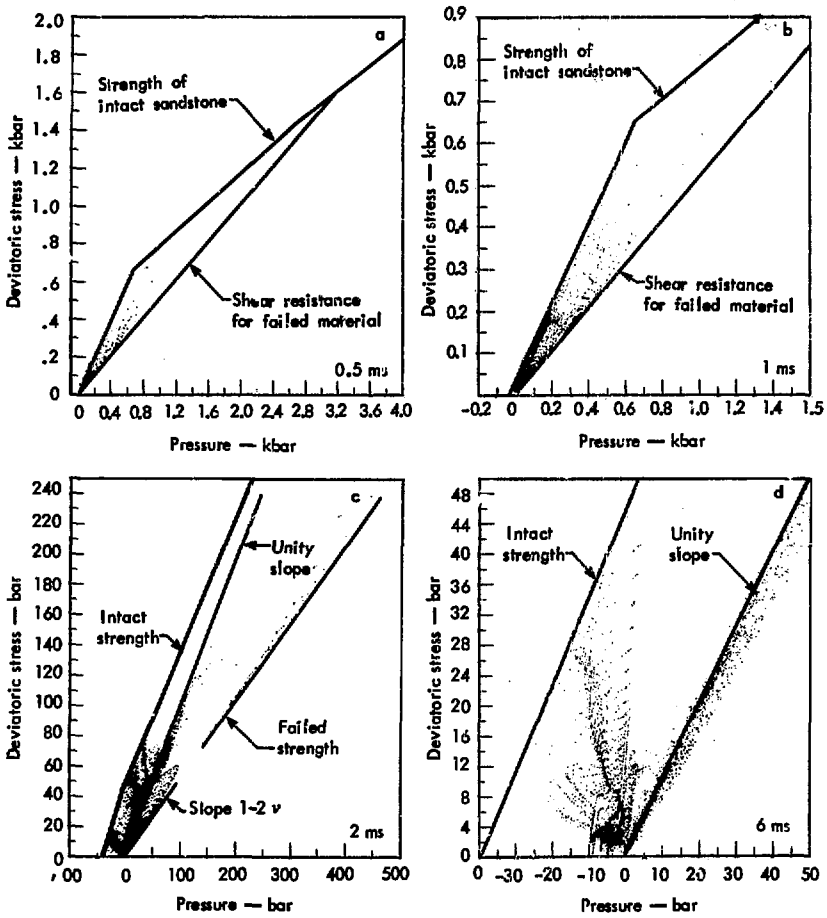

Fig. 25. Y-$\overline{P}$ points in calculation with uniform medium.

In this calculation, the value for Poisson's ratio for the sandstone was 0.24, giving a value of 0.52 for the slope of the 1 - 2ν one-dimensional strain Y-$\bar{P}$ line. This line intersects the Y-$\bar{P}$ failure surface for intact material at approximately 3 kbar, indicating that a plane compressive wave of this strength will reach compressive shear failure in the material. This slope value of 0.52 is almost equal to the slope of 0.513 for the line of shear resistance for completely failed material, but this is only a coincidence.

In Fig. 25a, at 0.5 ms, Y-$\bar{P}$ points are shown extending up to almost 4-kbar adjusted pressure. These points represent the failed zones that are near the burning explosive. Other points at lower pressures and deviatoric stresses may have already failed, since this plot represents instantaneous conditions rather than maximum values. At 1 ms (Fig. 25b), the peak pressures have decreased to approximately 1.5 kbar.

In Fig. 25c, the points have separated into several distinct groupings. The low-amplitude group on the right represents the outgoing stress wave, rising from the origin with a 1 - 2ν slope but being deflected to the left by the radial expansion. The peak pressure represented in this group is about 80 bar, in agreement with the pressure plot of Fig. 8d. Extending outward in this general direction is the group of points for the zones near the explosion, still at a residual high pressure. They appear to be constrained to lie near the line giving the shear strength for completely failed material. Using the criterion for complete failure, where the inelastic strain SV1 should be greater than 0.01, it is seen from the SV1 plots of Fig. 22 that there are many zones in this category.

The group of points on the extreme left are limited on the left by the failure line for intact material. These points have moved into the tensile region because of radial expansion, but the tensile stresses of all those that have crossed the failure surface have been relaxed to zero, moving the points to the right again.

The group of points lying along the line of unity slope represents zones that have diverged radially, so that the two transverse stresses have been reduced to zero. Most of these zones have passed through the tensile-failure routine, and in these zones no buildup of tensile stress again is permitted. There then remains only the compressive radial stress, corresponding to unconfined one-dimensional compression. These points must lie along this line of unity slope, as shown in Appendix C.

In Fig. 25d, the Y-$\bar{P}$ plot for 6.0 ms is shown on an expanded scale. By this time the dilatation stress wave has passed through all the zones in the complete mesh, leaving many zones under small residual deviatoric stress, but almost zero pressure. In this condition the compressive stresses are almost balanced by tensile stresses in other directions.

This separation of the Y-$\bar{P}$ points into well-defined groups is the result of different physical phenomena occurring in different parts of the grid. Failure tests and procedures are used to classify the failure types quantitatively to make the numerical calculations. In reality, the separation may not be this categoric.

Isometric Graphical Representation

Another form of TENPLT graphical output from the TENSOR74 calculations is the isometric representation of selected variables, which may aid in understanding the phenomena involved in rock mechanics application. Isometric plots are given in Fig. 26, showing the spatial variation of pressure, deviatoric stress Y, maximum compressional strain XMUS, and inelastic strain SV1 in three-dimensional form from the calculation with the uniform medium at 3 ms. In the pressure plot, the outgoing dilatational wave and the residual pressure near the explosive are visible. The ragged nature of the pressure near the explosive is caused by the breaking of the medium in a nonuniform manner, with irregular relaxation of the stresses. Note that Figs. 26a and 6f are different graphical representations of the same pressure field.

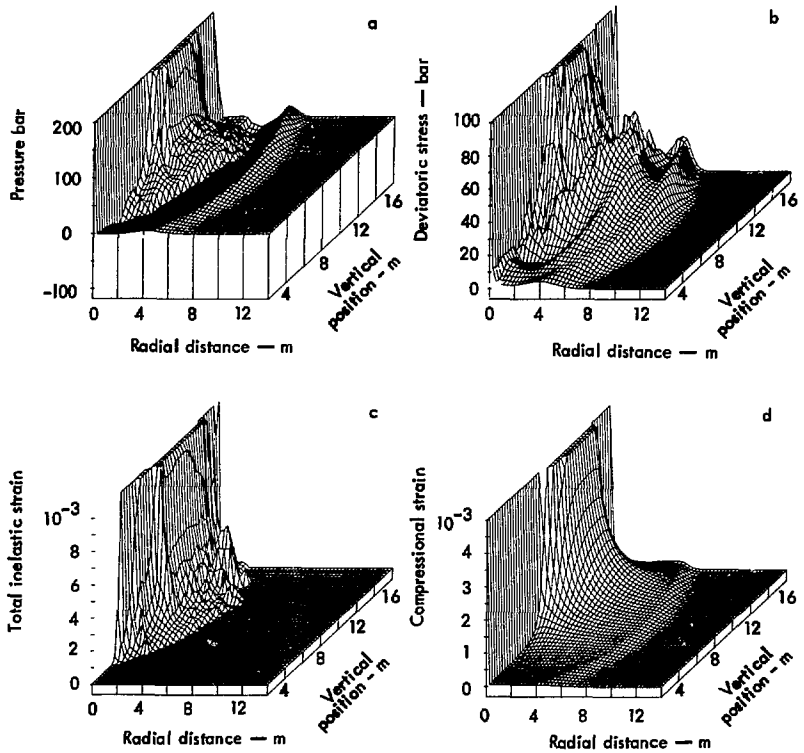

Fig. 26. Isometric representation of P, Y, SV1, and XMUS in uniform medium at 3 ms.

The plot giving the deviatoric stress Y shows both the dilatational wave and the shear wave following behind it. In regions of failed material, the deviatoric stresses are also rough in profile because of the dissimilar histories of the zones in the rock failure routines.

The inelastic strain SV1 shows the degree of rock damage that rises with discontinuous slope from the outer boundary giving the onset of rock failure. The plot of maximum compressional strain XMUS is smooth, since these values represent peak compression as the initial shock front passes through the intact material.

Effect of Reduced Tensile Strength of the Sandstone Medium

Significant differences often occur between properties of laboratory rock samples and bulk properties of undisturbed rocks in the field. Laboratory samples are ordinarily unfractured and homogeneous, while in the field these rocks may be less homogeneous and may contain joints or occur with bedding planes. These imperfections will ordinarily decrease the tensile strength below the values measured in the laboratory.

Since tensile failure represents a significant factor in the controlled blasting considered here, this uncertainty in the proper value of tensile strength to be used introduces major uncertainty into the expected volume and shape of the rock breakage pattern. A TENSOR74 calculation was made on which the input values for tensile strength at low values of deviatoric stress were reduced below those used in the reference calculation, as shown in Fig. 4. The resulting breakage pattern for this run was considerably larger than that for the reference run, as is evident on the comparative state plots of Figs. 20 and 23, and on the inelastic strain (SV1) plots of Figs. 22 and 24. The comparative amounts of failed rock were 1.59×10^6 kg at 5.5 ms for the standard case and 4.37×10^6 kg for the case of reduced tensile strength at the same time. The

Table 4. Comparison of amounts of failed rock and of radii of cracks in sandstone medium at 6 ms after initiation time.

Problem	Amount of failed rock (kg)	Approximate outer radius of radial cracks (m)
Reference problem	1.64×10^6	6.5
Tensile strength of sandstone medium reduced	4.37×10^6	9
ANFO explosive rather than gelled nitromethane	1.14×10^6	4.5
Top initiation rather than bottom initiation	1.78×10^6	6
Slip surface and buffer region included	1.44×10^6	5

tendency toward radial fracturing was also increased. These cracks for the low-strength case reached out approximately 9 m at 5.5 ms as compared with the value of 6.5 m for the reference problem. These comparative results are listed in Table 4. The increased extent of the tensile reflection breakage region near the surface has already been mentioned.

These figures on amounts of failed rock are obtained directly from the TENSOR74 calculations. The code lists as failed all those zones in which any inelastic relaxation has occurred and sums the mass in these zones. Some of this material may not be failed from an engineering point of view in that it may not be adequately broken up for easy removal.

It is concluded that the actual effective tensile strength is very important, and that a determination of the best value to be used in the calculations must be made by normalizing with the results from field tests.

Comparison of Results from Nitromethane and ANFO

For many engineering applications, ANFO is preferred over nitromethane as it is a less expensive explosive and has advantages in handling and storage. A

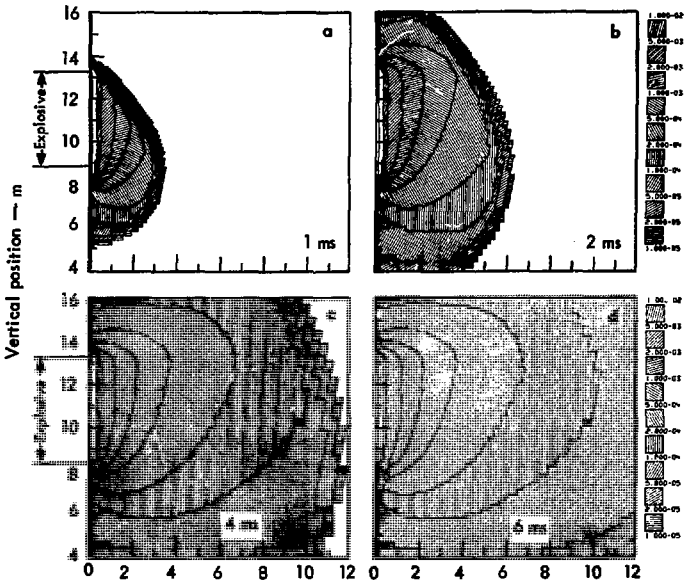

Fig. 27. Maximum compressional strain (XMUS) with ANFO explosive.

comparison of the properties of ANFO and of gelled nitromethane (as listed in Table 2) shows that ANFO is considerably less dense, has a lower detonation velocity, and has a lower energy output per cubic centimeter than gelled nitromethane. The energy release per gram of the two explosives is almost identical. A calculation was made in which the gelled nitromethane was replaced by an equal volume of the ANFO.

The resulting peak-compressional-strain (XMUS) plots are given in Fig. 27 for comparison with the plots of Fig. 21. It is seen that the peak strains are lower, as expected. Similarly, the total inelastic strain plots of Fig. 28 show that the inelastic strain is less, and that the volume of rock failure is considerably decreased from that shown in the corresponding plots for nitromethane as given in Fig. 21.

The total computed mass of failed sandstone at 6.1 ms for gelled nitromethane was 1.66×10^6 kg, while for ANFO the corresponding value was 1.14×10^6 kg at 6.0 ms. The rock breakage for the nitromethane was 2.21×10^4 kg per kilogram of explosive, while for ANFO the corresponding number was 2.37×10^4. These results imply that, with respect to the criterion of amount of rock breakage per unit mass of explosive, the two explosives are almost

Fig. 28. Total inelastic strain (SV1) with ANFO explosive.

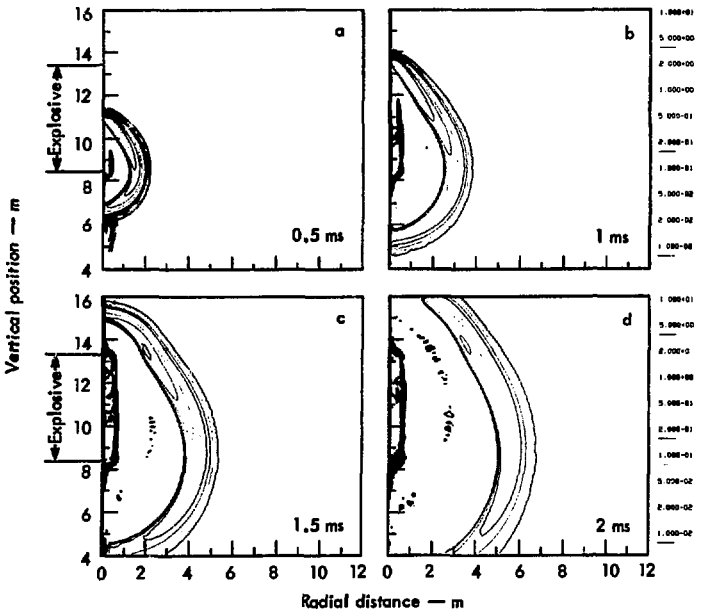

Fig. 29. Compressional phase of dilatational strain wave (DIVV NEG) with ANFO explosive.

equal. In this type of engineering application, the volume of explosive that can be used is limited to the volume of the emplacement hole. Consequently, the *criterion of effectiveness* per unit volume of explosive has practical significance.

Since ANFO has a lower detonation velocity than nitromethane, the shape of the outgoing stress wave is changed somewhat. The dilatational and shear waves at early times are shown in Figs. 29 and 30 respectively. As is listed in Table 3, the lower burn velocity of ANFO results in a greater angle between the direction of the outgoing stress wave and the axis.

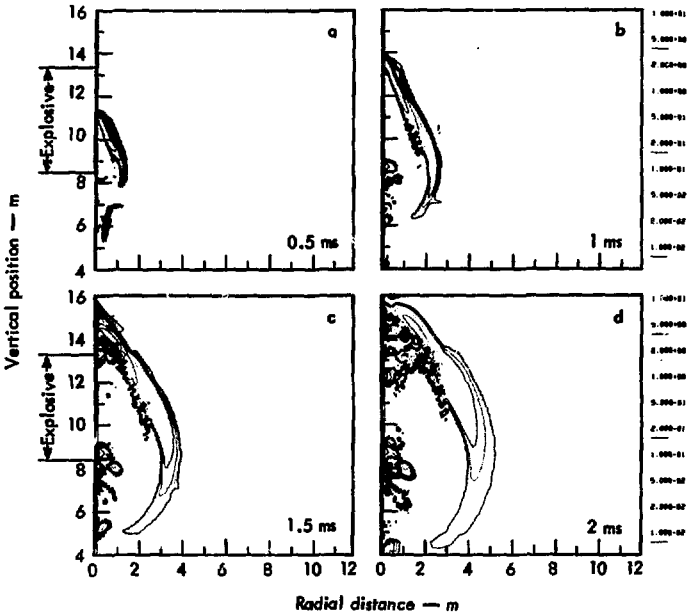

Fig. 30. Counterclockwise phase of shear wave (CURLV) with ANFO explosive.

Effect of Direction of Explosive Burn

A practical question in design of blasting geometries is the placement of the initiators. The location of these initiators determines the direction of burn of the explosive, which should have an effect on the timing and the direction of travel of the various segments of the outgoing stress waves. To study these effects, comparative runs were made with identical input in all respects except for the direction of burn of the explosive. The explosive considered was gelled nitromethane, with a detonation velocity of 6210 m/s, fired in the uniform sandstone medium with a sonic velocity of 2650 m/s.

The progress of the pressure wave at early times with top initiation of the explosive is shown in Fig. 31, for comparison with the corresponding plots with bottom initiation of Fig. 8. These plots show the conical emission discussed earlier. The two sets are similar but reversed in vertical direction until about 1 ms, when the stress wave reaches the surface of the medium. After this time the surface reflection introduces some dissimilarity. The DIVV NEG plots of

Fig. 32 gives an alternate picture of the stress-wave motion as compared with the plots in Fig. 10.

The quantity XMUS, which is the maximum strain value encountered in the history of the individual zones, is shown in Fig. 33, for comparison with the bottom-initiation case of Fig. 25. The directional effect near the explosive cylinder is pronounced, but at large radii, beyond about 10 m for this 4.9-m-explosive stick, this vertical directivity disappears. The contours become more nearly spherical at longer ranges, although some excess extension in the horizontal to the side of the explosive stick becomes evident. The quantity SV1, which is the cumulative inelastic strain acquired by the zone (see Fig. 34), shows less asymmetry because the stresses in the areas of constructive interference are higher but extend over a shorter time interval than the stresses in the other directions.

It is probable that the physical results of this directional effect are dependent upon the rock medium and upon the type of rock failure being considered. The higher directivity effects are associated with the higher stress levels, so that failure at higher values of Y and $\bar{P}$ (compressional failure) near the explosive should show stronger directional effects.

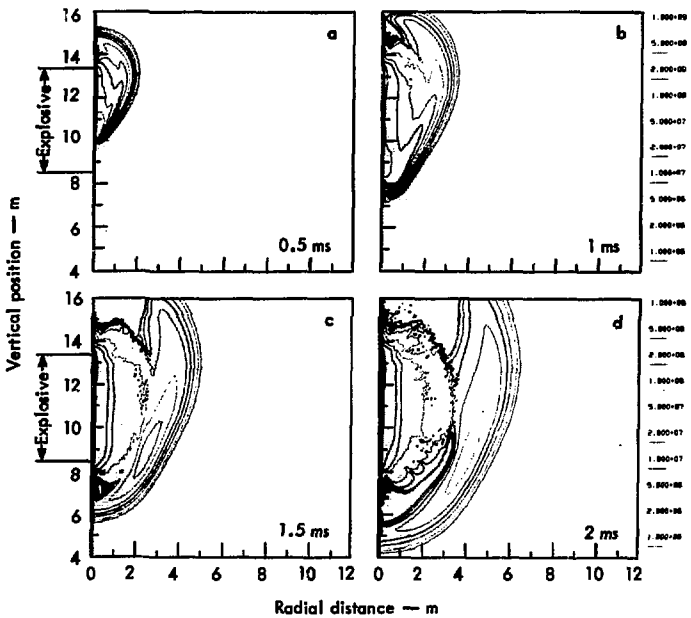

Fig. 31. Pressure in medium with top initiation of explosive stick.

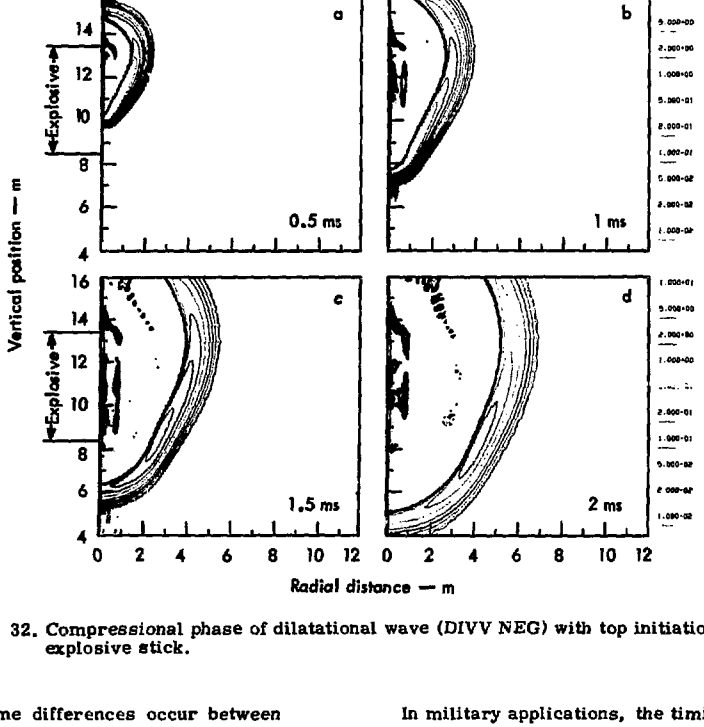

Fig. 32. Compressional phase of dilatational wave (DIVV NEG) with top initiation of explosive stick.

Some differences occur between the total inelastic curves of Fig. 34 and the corresponding curves of Fig. 21, where the explosive was initiated at the bottom. These results are somewhat inconclusive with respect to the effect on surface spall, however.

In military applications, the timing and the direction of explosive burn in shaped charges are of primary importance. It is concluded that in the less specialized applications in rock blasting, the direction of burn does not have a critical effect on the results, and that other considerations can control the placement of the initiation.

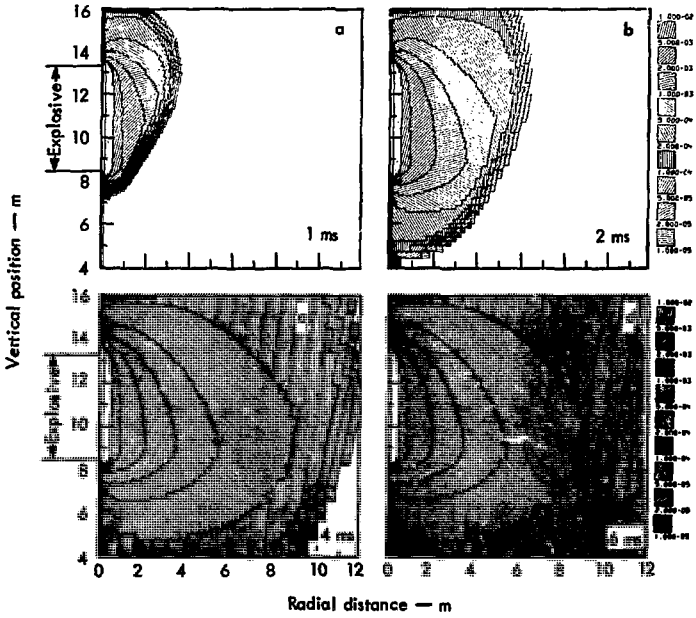

Fig. 33. Maximum compressional strain (XMUS) with top initiation of explosive stick.

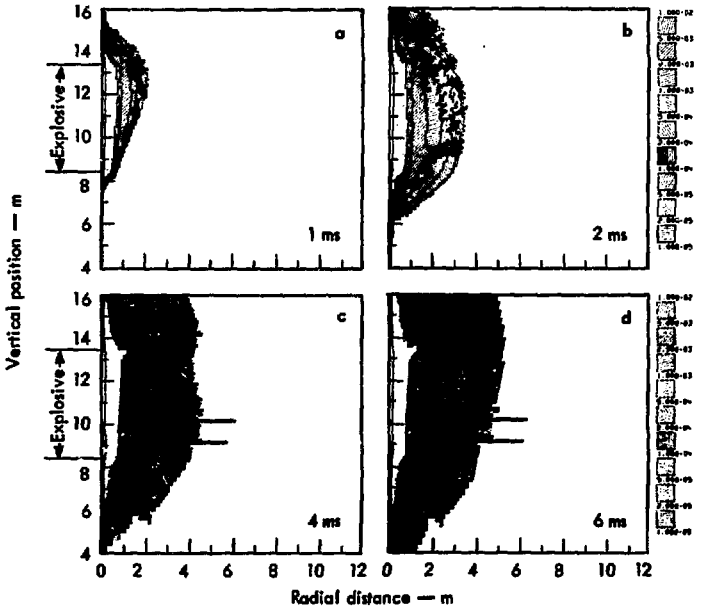

Fig. 34. Total inelastic strain (SV1) with top initiation of explosive stick.

Effect of Slip Surface and Buffer Region

In industrial excavation, the rock is sometimes prefractured along a particular plane to limit the rock failure region when the main charge is fired. Upon removal of the failed rock, a competent face of rock in the desired location will then remain. Buffer zones of crushed rock just inside the presplit surfaces may be used for better control of the fracture region. Computer calculations have been made here in such geometries both to explore the code capabilities and to contribute to better engineering design of these features.

The positions of the slip surface and of the buffer zone are shown in Figs. 7b, c, and d. The slip surface in the TENSOR calculations do not transmit lateral stress along the surface so that the media on the two sides are free to slide laterally, while the normal components of the stresses are transmitted directly. In field applications this may be somewhat unrealistic because lateral forces across a presplit plane probably do exist up to some limit as defined by frictional effects. This slip surface feature is required in TENSOR74, where large lateral motions

occur to preserve reasonable zone shapes and to decouple points across the surface that were originally close together, but which have subsequently moved far apart.

Several aspects of the reference calculation results in the uniform medium have already been discussed. The progressive enlargement of the failed region is shown in the state plots of Fig. 20. After about 2.5 ms the failed region appears to have acquired essentially its full size, although some radial cracks continue to grow. The maximum compressive strain plots XMUS and the inelastic strain SV1 are shown in Figs. 22 and 21 respectively.

When the slip surface was added at the location shown in Fig. 7b, the resulting pressure plots of Fig. 35 show only moderate change from the corresponding plots of Fig. 8. In directions where the stress wave strikes the slip plane normally, there is very little effect on the pressure, while at more grazing angles of incidence a larger effect is evident. Similarly, the negative phase of the divergence of the velocity as given in Fig. 36 shows only minor differences from the corresponding uniform field plot of Fig. 10. The maximum compressional strain plot (see Fig. 37) shows some effect of the slip surface, primarily at the upper and lower

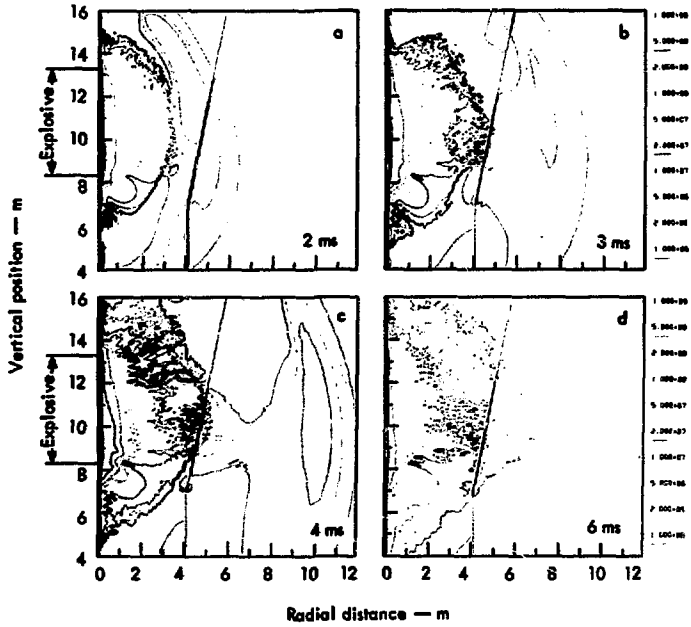

Fig. 35. Pressure in medium with slip plane.

ends. The total inelastic strain SV1 of Fig. 38 shows a significant effect of the slip surface in that the long-horizontal-progressive cracks are terminated by the surface. There is a small amount of failed material beyond the slip surface, but it appears to have been quite effective in limiting the region-of-rock failure.

The influence of the slip surface on the late particle motion, as shown in Fig. 1[illegible], is more pronounced. It appears that the entire conical region is in the process of ejection and that the rock face at the slip surface is remaining intact. Further information may be obtained by running the machine calculations to later times, although reflections are already r[illegible]ming from the outer boundary at 6 [illegible]s is evident in the strain rate plot of Fig. 10h.

The buffer region consisted of 42-cm-thick crushed sandstone, at the location shown in Fig. 7c. The outer edge of this region was at K = 52, in the same location as the slip surface of the preceding paragraphs.

The properties of this crushed material are listed in Table 1. In the calculations, this crushed material can sustain a deviatoric stress only up to that defined by the Y-$\bar{P}$ curve of Fig. 6, while the compressibility is greater than for the

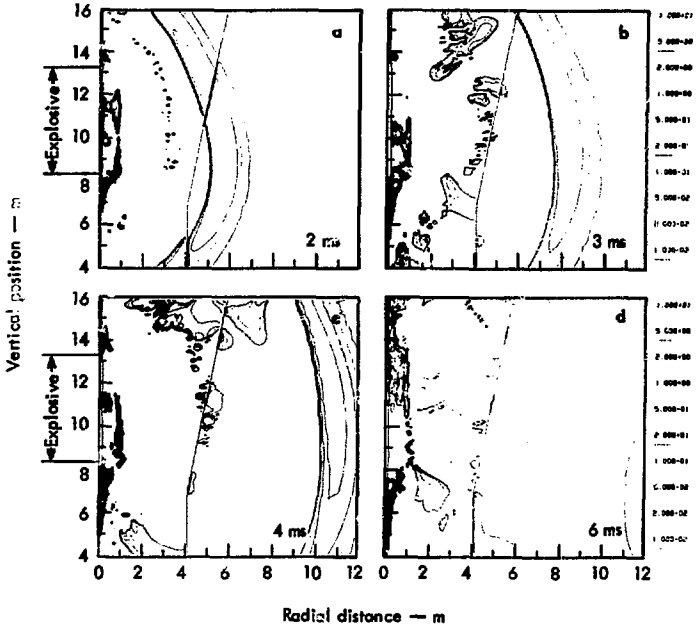

Fig. 36. Compressional phase of dilatational wave (DIVV NEG) in medium with slip surface.

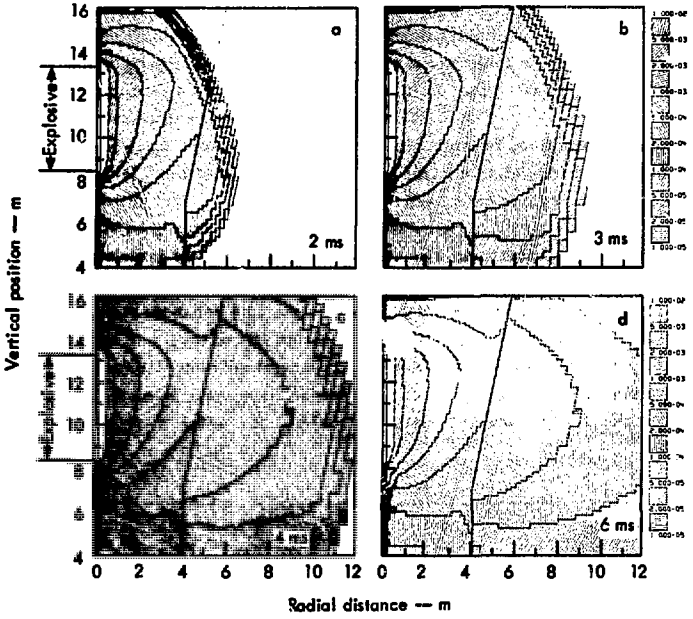

Fig. 37. Maximum compressional strain (XMUS) in medium with slip surface.

unfailed rock because of the air voids present, as is evident in the P-ξ graph of Fig. 5.

The pressure plots of Fig. 39 are qualitatively similar to the corresponding plots with the slip surface of Fig. 35, although lower pressures within the buffer zone itself and some broadening of the front beyond the buffer zone are apparent. Also the peak-compressive-strain plots of Fig. 40 are similar to those of Fig. 37. The buffer region also introduces a small time delay in the progress of the dilatational wave, this time being related to the higher compressibility and lower shock velocity of the rock. The buffer region appears to be slightly more effective than the slip surface in stopping the radial cracks, as is shown in the SV1 plots of Fig. 41. This observation is not definitive in terms of field design because the form and location of these two types of barriers are not optimized and may not be physically realistic. The peak pressure that is imposed upon the sand inside the buffer region is of the order of 100 bar, giving a compression ξ of approximately 0.001. This value of ξ is far below the value of 0.03 corresponding to complete closure of the void space, so it is concluded that the excess porosity of the sand is ineffective here in modifying the stress wave. A weaker, more crushable medium would have been more

effective in this application. The influence of the buffer zone is felt primarily through the lower value of bulk modulus and the lower resistance to shearing motion in the sand.

In engineering practice, presplit surfaces are often used for better control of blasting, and buffer regions have been proposed for further control. A calculation was made for such a combination with the slip surface again located at K = 52, about 5 m from the explosive, and with the 42-cm-wide buffer region spaced approximately 51 cm inside the slip surface, as is shown in Fig. 7d. The resulting pressure, XMUS, and SV1 plots are shown in Figs. 42, 43, and 44, respectively.

These results are not markedly different from those where only a slip surface or buffer region was used, although with this combination the progressive cracks appear to have been terminated more effectively. There is some indication that the compressible buffer zone acts as a low-impedance interface that sends a tensile reflection back into the inner rock region and enhances the early rock failure to the left of its inner surface; the slip plane alone does not appreciably enhance the early rock failure. These conclusions are valid only for this particular

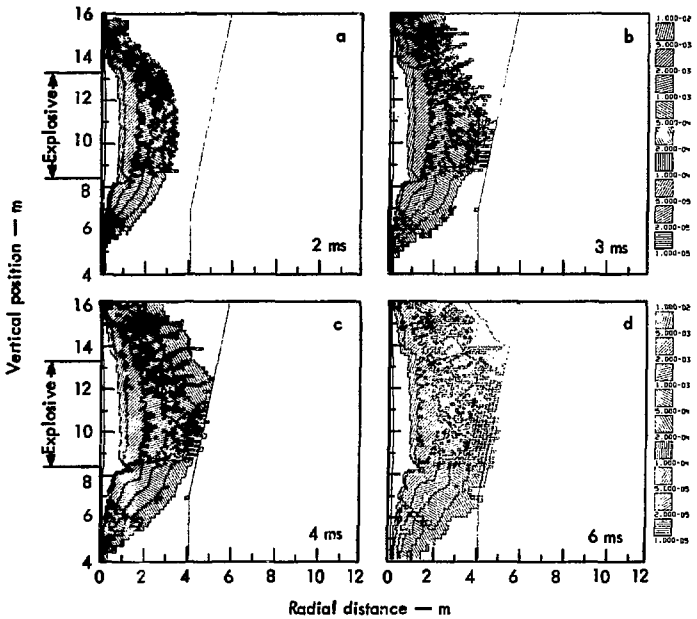

Fig. 38. Total inelastic strain (SV1) in medium with slip surface.

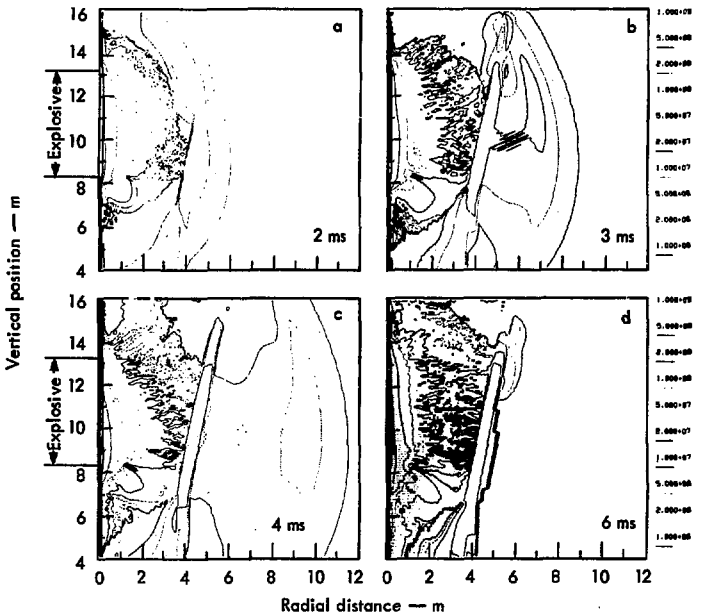

Fig. 39. Pressure in medium with buffer region.

experiment and further calculations must be made for applications in other media and geometries. In addition, the properties chosen for the buffer zones and slip surfaces may not be realizable in the field.

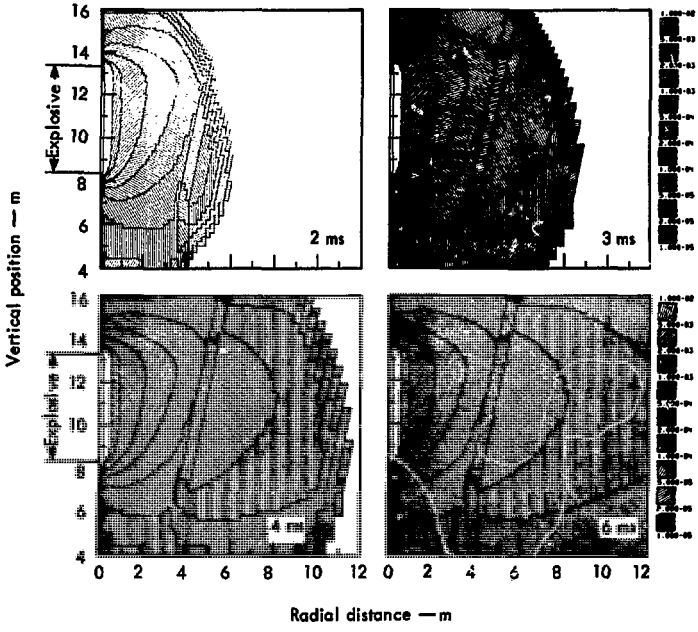

Fig. 40. Maximum compressional strain (XMUS) in medium with buffer region.

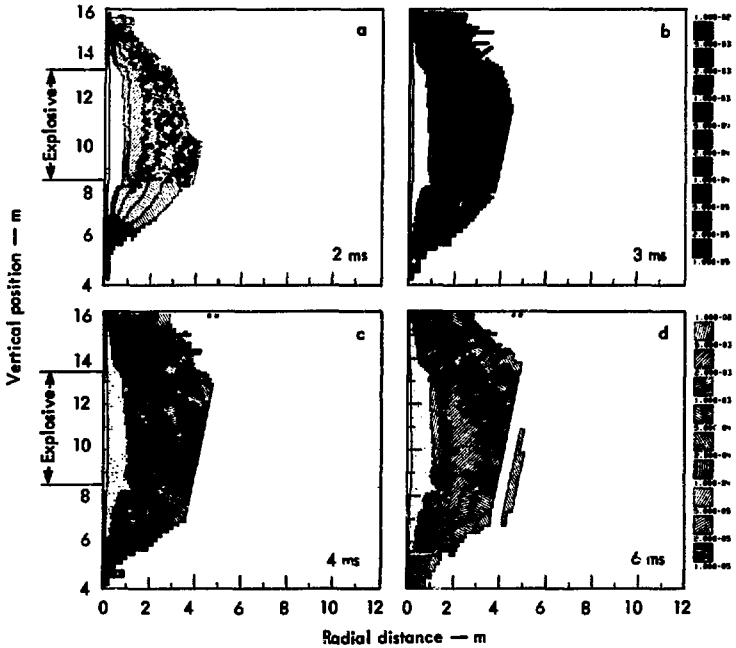

Fig. 41. Total inelastic strain (SV1) in medium with buffer region.

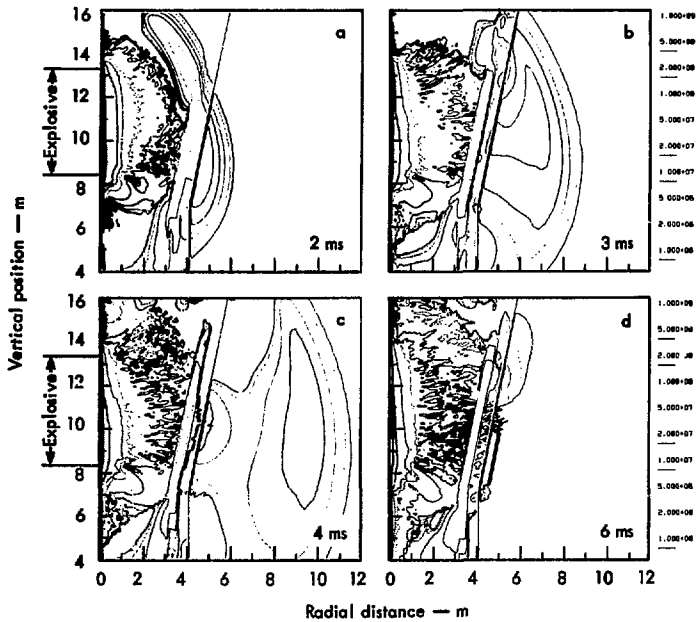

Fig. 42. Pressure in medium with slip surface and buffer region.

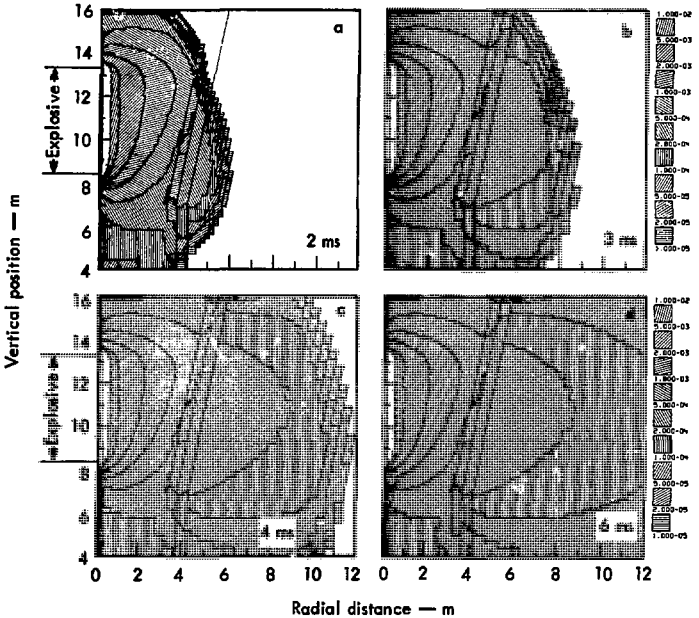

Fig. 43. Maximum compressional strain (XMUS) in medium with slip surface and buffer region.

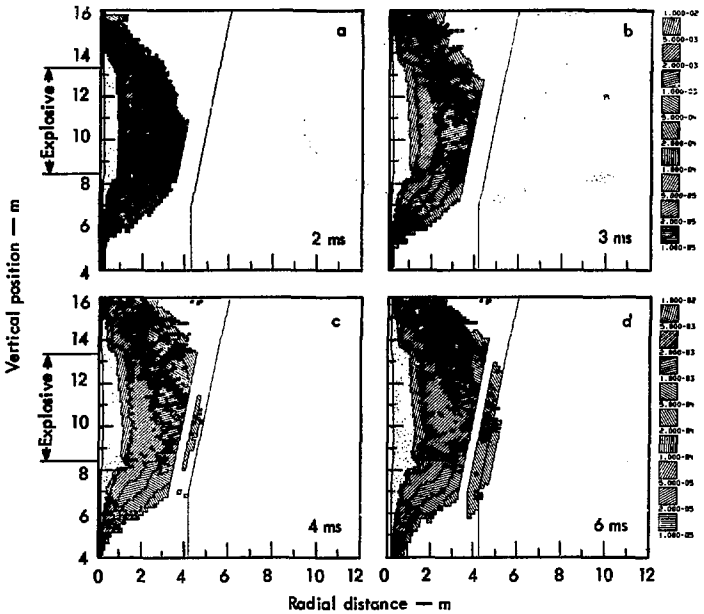

Fig. 44. Total inelastic strain (SV1) in medium with slip surface and buffer region.

Summary of Results

This report gives the results of TENSOR calculations on underground explosions with an energy source in the form of a vertical column initiated at one end. The double objective was to develop the calculation procedures and to obtain calculated results for interaction with field experiments. More attention was given to understanding the phenomena and identifying the difficulties than to supplying quantitative data for field applications. The problem was originally stated as controlling the rock failure pattern through the use of slip surfaces and buffer regions, but primary emphasis was placed on understanding the simpler case of a blasting application without these controls and on exploration of the calculational techniques.

These calculations appear to have been successful in showing the effects of buffer zones and slip planes in limiting the extent of damage from the explosions. The results show that these barriers tend to terminate radial cracks, and this aspect may be of decisive importance in the field.

The calculations have shown a marked directivity in the outgoing stress wave,

depending upon the direction of burn of the explosive. The directivity of the physical results depends upon the nearness of the explosive charge and upon the parameters being considered. Directivity is most evident for the transient shock-front parameters such as peak pressure. The final pattern of failed rock for the application considered here was not very sensitive to the direction of explosive burn, however.

A comparison of the size of the region-of-rock failure for the two explosives contained within the same borehole volume showed that nitromethane gave a larger volume of failed rock than ANFO, as was expected because of its higher total energy content. When the volume of failed rock was related to the total weight of the explosive, the ANFO explosive gave a slightly higher efficiency.

It has been found that the amount of rock failure in tension is very dependent upon the tensile strength of the rock. Radial cracks, resulting from tensile stresses created by the outward radial motion of the rock medium, are much more extensive with the rock with lower tensile strength. In addition, there is a larger amount of surface spall, although the failure patterns from the calculations do not give easily identified spall planes.

The TENPLT code has been used for graphical presentation of the TENSOR74 results. Graphical plots have been obtained for pressure, state of the media, maximum compression, total inelastic strain, vector velocity field, divergence and curl of the velocity, and other parameters. The position of the stress wave as a function of time has been presented, showing the progressive enlargement of the region-of-rock failure. The dilatational and shear waves have been isolated and presented in their generation, motion, and interaction with boundaries. Plots of some of the parameters in isometric form have provided a useful alternate form of data presentation.

The failure domains have been studied with the aid of the Y-$\bar{P}$ plots, and it is concluded that, at locations near the explosive, the medium fails in shear at high pressure. Further from the explosive, the medium fails in tension at low-confining pressure, the tensile stresses being primarily hoop stresses, although some tensile failure from surface spall is observed.

These results are interesting and informative, but they or similar calculations must be quantitatively verified by field experiments in media whose properties are known. Some of the areas in which there is considerable uncertainty are the following:

- The properties of the rock samples in the laboratory may not be representative of the properties in the field. This may occur because only competent rock samples are selected for laboratory testing. Discrepancies may also occur because the laboratory samples are small in scale, while large-scale properties are involved in field blasting. The large-scale tensile strength, an important property in blasting applications, may be lowered by the presence of joints and bedding planes.
- The calculated amount of fracturing depends upon the prescription used to describe the failure. Higher values of artificial viscosity and longer failure time constants reduce the calculated amount of failed material. In addition,

Dr. W. W. Hakala of NSF has served as program manager of this project.

Constructive criticisms on this report have been made by T. Ricketts (EERL), J. Hannon, and Barbara Crowley.

Cheerful typing and retyping has been done by Diane Taasevigen, and efficient editing has been done by Joan Hiraki of the Technical Information Department.

Appendix A — Material Failure in TENSOR74

Two different types of failure routines were used in the TEN31B version of the TENSOR74 program used for the calculations presented in this report. The first is the compaction of the medium, discussed here with the aid of Fig. 1. The material upon initial loading moves up along the P-ζ curve for intact material. If the loading does not go beyond the elastic limit ζ_1, the state of the material does not change, and the unloading path is back along the same line. If the loading goes beyond ζ_2, the material is assumed to be fully compacted, and the unloading path is along the compacted curve as shown, from ζ_2 to ζ_3.

When the loading is to some point ζ_m between ζ_1 and ζ_2, the unloading and subsequent reloadings follow an intermediate path.[33,8] For this intermediate path, a line is constructed parallel (equal slope at corresponding values of pressure) to the fully compacted curve. This line strikes the axis of zero pressure at some point ζ_r. From laboratory data, the actual residual compaction strain is expressed by the polynomial

$$\zeta_s = \zeta_3 (A_1 x + A_2 x^2 + A_3 x^3),$$

where

$$x = (\zeta_m - \zeta_1)/(\zeta_2 - \zeta_1)$$

and

$$A_1 + A_2 + A_3 = 1.$$

A correction term is added to the curve from ζ_m to ζ_r such that this curve will strike the point ζ_s by use of a linear correction of the slope α of this unloading line:

$$\frac{1}{\alpha} = \frac{1}{\alpha_c} + \frac{\zeta_r - \zeta_s}{P_m} .$$

The term α_c is the slope of the line for fully compacted material, and P_m is the pressure at compressional strain ζ_m. These slopes are measured along equal pressure levels.

Included in TENSOR74 is the phenomenon of bulking, in which the material that has failed in tension follows a new reloading P-ζ curve to the left of the intact material curve because of the irregular voids created. This bulking option was not used in these calculations.

The second type of failure included in TENSOR74 is the failure occurring when the Y-$\bar{P}$ points move outside of the failure envelope. This failure can be either in tension or in shear, and the shear failure can be either brittle or ductile. These failure types are discussed here with the aid of Fig. 2, showing failure envelopes for intact material, completely failed material, and partially failed material. These curves coincide at stresses beyond the brittle-ductile transition, indicating that beyond this point the resistance to shearing motion becomes independent of the previous history of the material.

The location of the envelope for partially failed material in the brittle region is dependent upon the amount of inelastic strain that the material has previously undergone. This line is constructed by interpolating Y linearly at given values of $\bar{P}$ between the intact and the completely failed envelopes:

$$Y_i = Y_0 - (Y_0 - Y_f)\epsilon/\epsilon_0 \quad \text{for } \epsilon < \epsilon_0,$$

$$Y_i = Y_f \quad \text{for } \epsilon \geq \epsilon_0.$$

The term Y_i is the point on the curve for partially failed material, Y_0 is on the

intact material curve, and Y_f is on the completely failed curve.

The value of the incremental inelastic strain $\delta\epsilon$ is the sum of the strains in shear and in tension:

$$\delta\epsilon = \left[\frac{1}{2\mu}|\delta I| + \frac{1}{K}|\delta P_t|\right].$$

The term δI is the inelastic shear relaxation, where I is the square root of the second deviatoric stress invariant, $I = \left[I_{2D}\right]^{1/2}$. The term δP_t is the pressure change at tensile failure, and μ and K are the incremental shear and bulk moduli. The reference strain ϵ_0 indicating complete failure is given a value of 0.01 here.

When the point crosses the Y-$\bar{P}$ curve in the ductile region, the deviatoric stresses are decreased by a common factor to move the point down to the curve in a single calculational cycle. In the brittle region the stress relaxation is given a time constant as is indicated in the following equation

$$S_i = \tilde{S}_i \left[1 - \frac{\delta t}{\tau}\left(\frac{\Delta Y}{\tilde{Y}}\right)\right].$$

Here the term $\tilde{S}_i$ denotes the deviatoric stresses as calculated from the previous cycle using the dynamic values for μ, K, and elastic motion, and δt is the increment of time covered in a cycle, τ is a time constant supplied as input to the problem, and $\Delta Y/\tilde{Y}$ is the distance that the point exceeds the particular applicable failure envelope divided by the elastically calculated value for the composite deviatoric stress Y. The new values of deviatoric stress for the next cycle are S_i.

For tensile failure, two separate relaxation rates were used in the TEN31B version of TENSOR74. When the Y-$\bar{P}$ point has crossed the failure surface, the principal stress largest in tension fails with a relaxation rate of

$$T_i = \tilde{T}_i \left(1 - \frac{\delta t}{\tau}\right).$$

The term T_i is the tensile stress as calculated for elastic motion and $\tilde{T}_i$ is the corrected tensile stress to be used in the next calculational cycle. Any other principal stress in tension fails at the slower rate of

$$T_i = \tilde{T}_i \left(1 - \frac{\delta t}{\tau}\frac{\epsilon}{\epsilon_0}\right).$$

The correction on the tensile stress per cycle in this case is decreased by the factor ϵ/ϵ_0, which becomes unity only for completely failed material. The most tensile stress is relaxed to zero, while if there is a second principal stress in tension, it is relaxed until the Y-$\bar{P}$ point reaches the failure surface effective for that zone.

After tensile failure has occurred, the medium is assumed to have zero tensile strength in the direction of that principal stress that had the greatest tension. It has a tensile strength as determined by the Y-$\bar{P}$ failure line in the other two directions. This is an incomplete treatment because it does not allow for changing angles of the direction of the principal stresses.

Appendix B — Scalar and Vector Fields

An equation in small-deformation linear-elasticity theory given by Navier[34] has the form

$$(\lambda + \mu)\,\nabla\,(\nabla \cdot \bar{u}) + \mu\,\nabla^2\bar{u} + \rho\bar{b} = \frac{\partial^2\bar{u}}{\partial t^2}.$$

The quantities λ and μ are the Lame constants, $\bar{b}$ is a body force, and $\bar{u}$ was originally defined as a displacement. In TENSOR74 calculations, the strain rate (time derivative of strain) is used rather than strain, so that in this equation it is more convenient to define $\bar{u}$ as velocity and $\bar{b}$ as the time rate of change of body forces. In this work, there are no time-varying body forces $\bar{b}$, so this term will be dropped.

By use of the vector identity $\nabla^2\bar{u} = \nabla(\nabla\cdot\bar{u}) - \nabla x\nabla x\bar{u}$, the Navier equation is converted to the form

$$(\lambda + 2\mu)\,\nabla\,(\nabla \cdot u) - \mu\nabla x(\nabla x u) = \rho\frac{\partial^2\bar{u}}{\partial t^2}.$$

In Helmholtz' representation,[35] a finite-continuous-vector field may be expressed as the following sum:

$$\bar{u} = \nabla\phi + \nabla x\bar{\alpha},$$

and this can be expressed as

$$\bar{u} = \bar{u}_\theta + \bar{u}_w,$$

where $u_\theta = \nabla\phi$ and $\bar{u}_w = \nabla x\bar{\alpha}$. The term ϕ is ordinarily called the scalar potential and $\bar{\alpha}$ the vector potential. Since the divergence of the curl and also the curl of the gradient is zero, $\nabla\cdot\nabla x\bar{\alpha} = 0$ and $\nabla x\nabla\phi = 0$, the equation of motion becomes

$$(\lambda + 2\mu)\,\nabla\,(\nabla\cdot\bar{u}_\theta) - \mu\nabla x(\nabla x\bar{u}_w) = \rho\frac{\partial^2(\bar{u}_\theta + \bar{u}_w)}{\partial t^2}.$$

The two velocity fields, $\bar{u}_\theta$ and $\bar{u}_w$, are thus uncoupled to give the two equations

$$(\lambda + 2\mu)\,\nabla\,(\nabla\cdot\bar{u}_\theta) = \rho\frac{\partial^2\bar{u}_\theta}{\partial t^2},$$

$$-\mu\nabla x(\nabla x\bar{u}_w) = \rho\frac{\partial^2\bar{u}_w}{\partial t^2}.$$

The vector identity $\nabla^2\bar{u} = \nabla(\nabla\cdot\bar{u}) - \nabla x\nabla x\bar{u}$ is again used here, converting these equations to the form

$$(\lambda + 2\mu)\,\nabla^2\bar{u}_\theta = \rho\frac{\partial^2\bar{u}_\theta}{\partial t^2},$$

$$\mu\nabla^2\bar{u}_w = \rho\frac{\partial^2\bar{u}_w}{\partial t^2}.$$

These are usual forms of the wave equation, with characteristic sonic velocities of $[(\lambda + 2\mu)/\rho]^{1/2}$ and $[\mu/\rho]^{1/2}$ respectively. The Lame constant λ is equal to $K - 2\mu/3$, where K is bulk modulus and μ is shear modulus, already appearing in the equations. This gives the sonic velocity for the $\bar{u}_\theta$ wave of $[(K + 4\mu/3)/\rho]^{1/2}$.

In the calculations, a composite velocity field $\bar{u}$ containing both the $\bar{u}_\theta$ and $\bar{u}_w$ parts is found. If the divergence operation is performed on the field $\bar{u}$,

only the $\bar{u}_\theta$ component will contribute to to the result, while if the curl operation is performed, only the $\bar{u}_w$ component will contribute:

$$\nabla \cdot \bar{u} = \nabla \cdot \bar{u}_\theta,$$
$$\nabla x \bar{u} = \nabla x \bar{u}_w.$$

The term $\nabla \cdot \bar{u}_\theta$ is the dilatational strain rate $\dot{\theta}$ as used in the code and the term $\nabla x \bar{u}_w$ is twice the rotation rate tensor. The velocity field $\bar{u}_\theta$ is identified as associated with dilatational or compressional waves, and the $\bar{u}_w$ field is associated with shear waves.

The boundary conditions are not amenable to this separation into the two independent fields, but instead this is the region where the two are highly coupled. Consequently, the boundaries or other irregularities in the otherwise uniform medium act as sources for the two fields, with the disturbances traveling outward with their characteristic velocities for the dilatational and the shear wave fields.

The case of the Rayleigh waves or other surface waves is interesting in that the dilatational and shear wave disturbances do not radiate away at their characteristic velocities. Instead they radiate downward into the medium with a high rate of attenuation, apparently not following the wave equation at all. An explanation is that for the dilatational waves, for example, although there are local areas of compression and of extension at the surface, there is no net dilatation. At large distances into the medium, the amplitude of the dilatational field decreases to zero through destructive interference of the various contributions. Nearer the surface, the geometric distribution of the sources permits local fields to exist. In other words, the monopole source is zero but higher order sources exist and create the observed fields. Similarly, for the shear wave field the total vorticity must be zero, although a local-shear-wave field exists because of the existence of higher order sources at the surface.

In seismic work it may appear that in the "near" zone the solutions do not satisfy the wave equations presented here, and that analysis of the $\bar{u}_\theta$ and $\bar{u}_w$ fields is inadequate to explain near field results. This is caused by the presence of higher order sources as discussed in the preceding paragraph, and does not present an exception to this analysis.

Appendix C — Relations Between Y and $\bar{P}$

The failure envelope for the sandstone medium is defined in terms of the quantities Y and $\bar{P}$, where Y is a generalized form of the shear stress and $\bar{P}$ is an adjusted form of the pressure, defined by the relations

$$Y = \left[\frac{3}{4} I_{2D}\right]^{1/2},$$

$$P = -\frac{I_1}{3} - \frac{1}{2}\left[\frac{1}{2} I_{3D}\right]^{1/3}.$$

The quantity I_1 is the first total stress invariant, I_{2D} is the second deviatoric stress invariant, and I_{3D} is the third deviatoric stress invariant. These invariants are defined by the relations

$$I_1 = \sigma_1 + \sigma_2 + \sigma_3,$$

$$I_{2D} = \frac{1}{6}\left[(\sigma_1 - \sigma_2)^2 + (\sigma_2 - \sigma_3)^2 + (\sigma_3 - \sigma_1)^2\right],$$

$$I_{3D} = (\sigma_1 - s)(\sigma_2 - s)(\sigma_3 - s).$$

The quantities σ_1, σ_2, and σ_3 are the principal stresses, and s is the negative of the pressure, $s = (\sigma_1 + \sigma_2 + \sigma_3)/3 = 1/3\ I_1 = -P$.

The variables Y and $\bar{P}$ are used in failure specifications because equations using these variables reduce to the desired forms in one-dimensional calculations, and because they provide a useful symmetry between tensile and compressive stresses.[6,36]

The general stress-strain equations for a linearly elastic medium are the following:

$$\sigma_1 = (\lambda + 2\mu)\epsilon_1 + \lambda\epsilon_2 + \lambda\epsilon_3,$$

$$\sigma_2 = \lambda\epsilon_1 + (\lambda + 2\mu)\epsilon_2 + \lambda\epsilon_3,$$

$$\sigma_3 = \lambda\epsilon_1 + \lambda\epsilon_2 + (\lambda + 2\mu)\epsilon_3.$$

When a plane wave passes through the medium in the direction of σ_1, the medium is strained only in this direction, so that ϵ_2 and ϵ_3 are zero. This gives the simpler equations

$$\sigma_1 = (\lambda + 2\mu)\epsilon_1,$$

$$\sigma_2 = \sigma_3 = \lambda\epsilon_1.$$

The transverse stress is then related to the longitudinal stress by the equation

$$\sigma_2 = \sigma_3 = \frac{\lambda}{\lambda + 2\mu}\sigma_1 = \frac{1}{1 + \frac{2\mu}{\lambda}}\sigma_1.$$

By setting σ_2 and σ_3 equal to zero in the stress matrix, the quantity $2\mu/\lambda$ can be shown to be equal to $1 - 2\nu/\nu$, where ν is Poisson's ratio, which is equal to ϵ_2/ϵ_1 here, so that an alternate form of this relation is

$$\sigma_2 = \sigma_3 = \frac{\nu}{1 - \nu}\sigma_1.$$

This relation is then used in the expressions for I_1, I_{2D}, I_{3D}, Y and $\bar{P}$, giving the results

$$I_1 = \left(\frac{1 + \nu}{1 - \nu}\right)\sigma_1,$$

$$I_{2D} = \frac{1}{3}\left(\frac{1 - 2\nu}{1 - \nu}\right)^2 \sigma_1^2,$$

$$I_{3D} = \frac{2}{27}\left(\frac{1 - 2\nu}{1 - \nu}\right)^3 \sigma_1^3,$$

and

$$Y = \frac{1}{2}\frac{1-2\nu}{1-\nu}\sigma_1,$$

$$\overline{P} = \frac{1}{2}\frac{1}{1-\nu}\sigma_1.$$

The ratio of Y to $\overline{P}$ is

$$\frac{Y}{\overline{P}} = 1 - 2\nu .$$

This is the slope that should be expected on the Y-$\overline{P}$ plots for the passage of the initial stress wave, before subsequent radial motion has introduced hoop stresses.

When the material has failed, it will sustain no tensile stresses. If spherically divergent expansion occurs, tensile failure will occur in the two transverse directions, leaving only the compressive longitudinal stress. The resulting Y-$\overline{P}$ slope is calculated as follows:

$$\sigma_2 = \sigma_3 = 0 ,$$

$$I_1 = \sigma_1$$

$$I_{2D} = \frac{1}{3}\sigma_1^2,$$

$$I_{3D} = \frac{2}{27}\sigma_1^3 ,$$

$$Y = \left[\frac{3}{4} I_{2D}\right]^{1/2} = \frac{\sigma_1}{2},$$

$$\overline{P} = -\frac{I_1}{3} - \frac{1}{2}\left[\frac{1}{2} I_{3D}\right]^{1/3} = -\frac{\sigma_1}{2}.$$

In the compressive region, the numerical value for $\overline{P}$ is positive, and the deviatoric stress variable Y is always assumed positive, so that a positive slope of unity results:

$$\frac{Y}{\overline{P}} = 1 .$$

References

1. U. Langfors and B. Kihlstrom, The Modern Technique of Rock Blasting (Wiley, New York, 1963).
2. C. H. Johansson and P. A. Person, Detonics of High Explosives (Academic Press, London and New York, 1970).
3. Task Group for Mechanics of Solids, Office of Research and Development Presplitting, a Controlled Blasting Technique for Rock Cuts, U.S. Department of Commerce, Bureau of Public Roads, United States Government Printing Office, Washington, D.C. (July 1966).
4. D. E. Burton and J. Lattery, "Controlled Blasting Technology in Urban Excavation," presented at the Spring Hill Conf. Res. in Tunneling Excavation Technol. (Wayzata, Minnesota, September 14, 1973), unpublished.
5. M. Wilkins, "Calculation of Elastic-Plastic Flow," in Methods in Computational Physics, Vol. 3, Fundamental Methods in Hydrodynamics (Academic Press, London and New York, 1964).
6. J. F. Schatz, The Physics of SOC and TENSOR, Lawrence Livermore Laboratory, Rept. UCRL-51352 (1973).
7. J. T. Cherry and F. L. Petersen, "Numerical Simulation of Stress Wave Propagation from Underground Nuclear Explosions," in Amer. Nucl. Soc. Symp. on Eng. with Nucl. Explosives (Las Vegas, Nevada, January 1970), vol. 1.
8. J. F. Schatz, SOC73, An Improved One-Dimensional Wave Propagation Code for Rock Media, Lawrence Livermore Laboratory, Rept. UCRL-51689 (1974).
9. W. D. Schulz, "Two-Dimensional Lagrangian Hydrodynamic Difference Equations," Methods in Computational Physics, Vol. 3, Fundamental Methods in Hydrodynamics (Academic Press, London and New York, 1964).
10. G. Maenchen and S. Sack, "The TENSOR Code," in Methods in Computational Physics, Vol. 3, Fundamentals in Hydrodynamics (Academic Press, London and New York, 1964).
11. J. T. Cherry, S. Sack, G. Maenchen, and V. J. Kransky, Two-Dimensional Stress-Induced Adiabatic Flow, Lawrence Livermore Laboratory, Rept. UCRL-50987 (1970).
12. D. E. Burton and J. F. Schatz, Lawrence Livermore Laboratory, Internal Document RKCD 74-18 (1974). Readers outside the Laboratory who desire further information on LLL internal documents should address their inquiries to the Technical Information Department, Lawrence Livermore Laboratory, Livermore, California 94550.
13. T. R. Butkovich, J. Geophys. Res. 70 (4), 885 (February 15, 1965).
14. R. W. Terhune, T. F. Stubbs, and J. T. Cherry, "Nuclear Cratering on a Digital Computer," in Amer. Nuc. Soc. Symp. on Eng. with Nucl. Explosives (Las Vegas, Nevada, January 1970), vol. 1.

15. R. W. Terhune and J. G. Shaw, Calculation of Rock Fracturing from Multiple Nuclear Explosive Sources, Lawrence Livermore Laboratory, Rept. UCRL-74017 (1972); prepared for submission to IAEA Panel on Peaceful Uses of Nuc. Explosives (Vienna, Austria, 1972).
16. D. E. Burton, C. M. Snell, and J. B. Bryan, Computer Design of High-Explosive Experiments to Simulate Subsurface Nuclear Detonations, Lawrence Livermore Laboratory, Rept. UCRL-75190, (December 1973); (accepted for publication in Nucl. Technol.).
17. J. Lattery, "Hydrodynamic Computer Code Solution of Explosive Excavation Design Problems," in Army Numerical Analysis Conference (Frankfort Arsenal, Philadelphia, PA, February 1974).
18. D. E. Burton and C. M. Snell, User's Guide to: TENPLT (Tensor Graphics Code) and EOSLIB and XMUPGENS (Auxiliary Data Codes), U.S. Army Engineer Waterways Experiment Station Explosive Excavation Research Laboratory, Livermore, CA, Rept. MP-E-74-1 (March 1974).
19. T. R. Butkovich, A Technique for Generating Pressure-Volume Relationships and Failure Envelopes for Rocks, Lawrence Livermore Laboratory, Rept. UCRL-51441 (1973).
20. B. B. Redpath, Project Trinidad, Explosive Excavation Tests in Sandstone and Shale, U.S. Army Engineer Waterways Experiment Station Explosive Excavation Research Laboratory, Livermore, CA, Rept. TR-E-73-1 (July 1972).
21. R. Holmes, Explosive Excavation Research Laboratory, private communication (1973).
22. P. Turner, Lawrence Livermore Laboratory, private communication (1973).
23. E. L. Lee, H. C. Hornig, and J. W. Kury, Adiabatic Expansion of High Explosive Detonation Products, Lawrence Livermore Laboratory, Rept. UCRL-50422 (1968).
24. E. Lee, M. Finger, and W. Collins, JWL Equation of State Coefficient for High Explosives, Lawrence Livermore Laboratory, Rept. UCID-16190 (1973).
25. M. Finger, Lawrence Livermore Laboratory, private communication (1974).
26. E. Lee and M. Finger, Lawrence Livermore Laboratory, private communication (March 5, 1974).
27. J. M. O'Connor, et al., Explosive Selection and Fallout Simulation Experiments: Device Simulation (Project DIAMOND ORE), U.S. Army Engineer Waterways Experiment Station Explosive Excavation Research Laboratory, Livermore, CA, Rept. TR-E-73-102 (1973).
28. J. W. Dally, W. L. Fourney, and D. C. Holloway, A Dynamic Photoelastic Investigation of Explosive Induced Fracture, Department of Mechanical Engineering, University of Maryland, College Park, Maryland (September 1973).
29. W. L. Fourney, J. W. Dally, and D. C. Holloway, Int. J. Rock Mech. Min. Sci. and Geomech Abstr. 11, 393-401 (1974).

30. J. A. Viecelli, J. Comp. Phys. 12, 187-201 (1973).
31. R. N. Schock, H. C. Heard, and D. R. Stephens, J. Geophys. Res. 78, 5922 (1973).
32. D. D. Porter, Mining Congr. J. vol. 41-43 (January 1974).
33. R. W. Terhune, D. R. Stephens, and F. Petersen, Lawrence Livermore Laboratory, Internal Document UOPKL 72-46 (1972).
34. L. E. Malvern, Introduction to the Mechanics of a Continuous Medium (Prentice-Hall, Inc., Englewood Cliffs, New Jersey, 1969).
35. R. Aris, Vectors, Tensors, and the Basic Equations of Fluid Mechanics, (Prentice-Hall, Inc., Englewood Cliffs, New Jersey, 1962).
36. J. W. White, J. Geophys. Res. 78, 2438-2441 (1973).